Universidade de Aveiro Departamento de Física
2008

Amsalu Mute Soboki

Cresimento, Caracterização Estrutural e Óptica de Nanofios de ZnO

Growth, Structural and Optical Characterization of ZnO Nanowires

EMMS-Joint European Masters programme in Materials Science

Universidade de Aveiro Departamento de Física
2008

Amsalu Mute Soboki

Cresimento, Caracterização Estrutural e Óptica de Nanofios de ZnO

Growth, Structural and Optical Characterization of ZnO Nanowires

Dissertação apresentada à Universidade de Aveiro para cumprimento dos requisitos necessários à obtenção do grau de Mestre em Ciências dos Materiais, realizada sob a orientação científica do Doutora Teresa Monteiro, Professora Associada do Departamento de Física da Universidade de Aveiro e Doutor Lars Rosgaard Jensen, Assistente Professor do Departamento de Engenharia Mecânica da Aalborg Universitet.

A dissertation presented to the University of Aveiro in partial fulfilment of the requirements for the awarding of the Joint European Master degree in Materials Science carried out under the supervision of Professor Teresa Monteiro, Associate Professor of Physics Department of University of Aveiro and Dr. Lars Rosgaard Jensen, Assistant Professor of Mechanical Engineering Department of Aalborg University.

Financial support from Erasmus Mundus Programme

Dedicated to my wife and my daughter for their patience and tireless support.

o júri

Presidente

Prof. Dr. Vítor Brás de Sequeira Amaral
Professor Associado com Agregação do Departamento de Física da Universidade de Aveiro

Prof. Dr. Tito da Silva Trindade
Professor Associado do Departamento de Química da Universidade de Aveiro

Prof. Dra.Teresa Maria Fernandes Rodrigues Cabral Monteiro
Professor Associado do Departamento de Física da Universidade de Aveiro

Prof. Dr. Eduardo Jorge da Costa Alves
Investigador Principal Responsável do Instituto Tecnológico e Nuclear

Acknowledgments

First, I would like to express my sincere appreciation to my advisors, Prof. Teresa Monteiro and Prof. Lars Rosgaard Jensen, for their wonderful guidance and support during this thesis work. They demonstrated their expertise towards the realization of this thesis work. They also gave me wonderful lectures during my study. I am happy to be associated with them.

My gratitude also extends to Thelge Chaminda for his cooperation during the growth process, to Marco Peres for his support during the optical characterization and helpful discussion of the results, and to Rosario Soares for her assistance in the XRD measurement.

I would like to thank the staffs in the spectroscopy research group of the I3N Laboratory from the Physics Department of University of Aveiro (UA) for their assistance during my stay with them in the laboratory and for letting me use the instruments for the optical characterization. I am also thankful to Mr. Francisco Reis for his technical assistance throughout my stay for the masters study at UA.

I would like to express my deepest love, respect, and admiration to all my family for their unconditional support, understanding, and dedication throughout my study. More specifically, I am thankful to my wife, Abebech, and my daughter, Sena, for the love, inspiration and unknowing support they offered me and for their patience during this master course.

My profound gratitude also goes to the European Commission for the financial support under the scheme of Erasmus Mundus programmme and the universities involved in the EMMS program for their support.

Last but not least, I want to express my warm feelings to all my EMMS friends for we were one happy family during the course.

palavras-chave

ZnO, nanofios, evaporação térmica, dispersão Raman, fotoluminescência, excitões.

resumo

Nanofios de ZnO foram crescidos por evaporação térmica na presença de um fluzo de oxigénio em substratos de alumina. O crescimento foi efectuado à pressão ambiente e sem a utilização de catalisadores externos. Identificou-se que o gradiente de temperatura entre o material de base e o substrato constitui o factor determinante no rendimento e tamanho dos nanofios. A utilização de microscopia electrónica de varrimento (SEM) revelou que as amostras, sujeitas a esta metodologia de crescimento, consistem em ZnO em volume que cresceu em cima da superfície do substrato a partir do qual crescem nanofios. A partir da morfologia observada sugere-se que o mecanismo de crescimento seja governado pela variação da super saturação do vapor de zinco durante o processo de crescimento. Foram realizadas medidas de difracção de raios-X (XRD) de modo a identificar a fase cristalina dos nanofios. A investigação das propriedades ópticas das amostras foi efectuada utilizando espectroscopia de Raman e fotoluminescência. Em dispersão Raman o aparecimento do modo E_2 (high) permitiu confirmar a cristalinidade dos nanofios com fase wurtzite hexagonal. Sob excitação banda a banda, o espectro de fotoluminescência registado a baixas temperaturas permitiu identificar que a recombinação óptica é dominada por excitões ligados a dadores ~ 3.37 eV. Foi também observada a emissão de excitões livres, emissão esta que é detectada até à temperatura ambiente. A observação das emissões excitónicas e a fraca intensidade das emissões relacionadas com defeitos profundos atestam a elevada qualidade óptica dos nanofios crescidos por esta metodologia.

keywords

ZnO, nanowires, thermal evaporation, Raman scattering, photoluminscence, excitons.

Abstract

Zinc oxide nanowires have been grown on alumina substrate by thermal evaporation of zinc powder in the presence of oxygen flow. The growth was performed at ambient pressure and without the use of foreign catalyst. Temperature gradient between the source material and substrate, in the favourable growth temperature region, was identified as key factor determining the yield and size of the nanowires. Scanning electron microscopy (SEM) observation showed that the as-grown sample consists of bulk ZnO crystal on the substrate surface with nanowires growing from this base. Growth mechanism of the observed morphology is suggested to be governed by the change of zinc vapour supersaturation during the growth process. X-ray diffraction (XRD) measurement was used to identify the hexagonal crystalline phase of the nanowires. Optical properties of the nanowires were investigated using Raman scattering and photoluminescence (PL). The appearance of dominant, Raman active E_2 (high) phonon mode in the Raman spectrum has confirmed the good cristallinity with wurtzite hexagonal phase of the nanowires. With above bandgap excitation the low temperature PL recombination is dominated by sharp donor bound exciton luminescence at ~3.37 eV. Free exciton emission is also seen at low temperature and can be observed up to room temperature. The optical data indicates that the grown nanowires have high optical quality.

Table of contents

List of tables

List of figures

List of abbreviations

A^0X	Exciton bound to neutral acceptor
CCD	Configuration coordinate diagram
CL	Cathodoluminescence
CVD	Chemical vapor deposition
CVTC	Chemical vapor transport and condensation
D^+X	Exciton bound to ionized donor
D^0X	Exciton bound to neutral donor
DAP	Donor-acceptor pair
E_{ex}^b	Free exciton binding energy
EC	Exciton complex
E_{loc}	Exciton localization energy
EMA	Effective mass approach
FX	Free exciton
FXA	Free exciton A
FXB	Free exciton B
LA	Longitudinal acoustic phonon
LO	Longitudinal optical phonon
MBE	Molecular beam epitaxy
m_e	Effective mass of hole
m_h	Effective mass of electron
MOCVD	Metalorganic chemical vapor deposition
PL	Photoluminescence
PR	Photoreflectance
PVD	Physical vapor deposition
RF	Radio frequency
RS	Raman spectroscopy
RT	Room temperature
SEM	Scanning electron microscopy
TA	Transverse acoustic phonon
TES	Two-electron satellite
TO	Transverse optical phonon
UV	Ultraviolet
VLS	Vapor-liquid-solid
V_O	Oxygen vacancy
VS	Vapor-solid
V_{Zn}	Zinc vacancy
XRD	x-ray diffraction
Zn_i	Interstitial zinc

CHAPTER 1: Introduction

Semiconductor nanowires as one-dimensional structures and components for nano-dimensional devices have gained increasing attention. Recently, various semiconductor nanowires, nanorods and nanotubes of single element, oxide and compound semiconductors have been successfully synthesized. The progress in growth of these nanostructures has led to the first successful production of devices based on nanoscale semiconductors [1,2]. With the reduction of size into nano-scale, materials display novel electrical transport, optical, mechanical and thermal properties as a result of surface and confinement effects. In this regard, one-dimensional nanostructures are ideal candidates for investigating the dependence of these fundamental properties on the size and dimensionality.

Among the wide range of semiconductor nanomaterials, nanostructures of II-VI semiconductor zinc oxide (ZnO) has gained special interest due to its unique properties and versatile applications in transparent electronics, ultraviolet (UV) light emitters, piezoelectric devices, chemical sensors and spin electronics [1,2]. As compared to other transparent conducting oxides, ZnO is probably the most studied material due to its potential technological application as a result of the following interesting properties [3]. ZnO has a wide bandgap of 3.37 eV at room temperature (RT) combined with large free exciton binding energy (60 meV) that has vast application in electronic, optoelectronic, and optical applications. In order to achieve efficient excitonic laser action at RT, the binding energy of the exciton must be larger than the thermal energy at RT (26 meV). In this regard, the large free exciton binding energy of ZnO can ensure an efficient excitonic emission at RT, and hence can facilitate low-threshold stimulated emission at RT. In addition, ZnO is a unique multifunctional oxide in having semiconducting, piezoelectric and pyroelectric properties and is an ideal candidate for fabricating electromechanical coupled devices such as actuators [1,4]. It has been also identified that ZnO exhibits sensitivity to various gaseous species such as ethanol, acetylene, and carbon monoxide, which makes it suitable for sensing application [5]. Moreover, ZnO is a biodegradable and possibly biocompatible material suitable for medical and biomedical application without coating [4]. Zinc oxide has O^{2-} and Zn^{2+} terminated polar surface. Thus, the electrostatic interaction energy and the distinct chemical activities of the polar surfaces results in the

formation of a wide range of nanostructures by simple modification of the growth conditions. Added to this, ZnO is chemically stable and environmentally friendly material. Based on these outstanding physical properties and the stimulation towards device miniaturization, large effort has been focused on the synthesis, characterization and devices application of ZnO nanomaterials. In fact, different devices require large scale and controlled synthesis of nanostructures, and hence it is essential to find experimental conditions under which the desired nanostructures with better properties can be synthesized in large quantities, reproducibly, with controlled morphology.

In the past few years, a variety of fabrication methods including metalorganic chemical vapour deposition (MOCVD), chemical vapour deposition (CVD), physical vapour deposition (PVD), molecular beam epitaxy (MBE), thermal evaporation and condensation, etc. have been used to synthesis one-dimensional ZnO nanostructures. Moreover, various mechanisms such as vapour-liquid-solid (VLS), Vapour-solid (VS), and redox reaction were proposed to understand the growth of nanostructures [6,7]. Most of these synthesis techniques use metal catalysts, such as Au, Cu, Sn or other additives such as, NiO, Ga, to enhance and control the growth process [8, and references therein]. Recently, catalyst-free synthesis of ZnO nanostructures using thermal evaporation technique, which has gained most attractiveness to synthesis oxide nanowires due to its simplicity and low cost, has been also reported in literature [7,9,10,11]. On the other hand, the growth of ZnO by vapor deposition is typically affected by temperatures of the source and the substrate, the distance between the source and substrate, the carrier gas flow rate, pressure, tube diameter and starting materials [5,9,12]. The effect of these factors on the evolution of nanostructures has been studied by several authors [6,9,10,12]. However, majority of the works done so far are catalyst-assisted and/or involves low deposition pressure and little work is done on catalyst-free synthesis of ZnO nanowires under ambient pressure. On the other hand, the catalysts may introduce foreign impurity in the composition of the nanostructures, and the deposition pressure is known to affect the vapour supersaturation level which is crucial to determine the type of growth to occur. Therefore, there is a need to further explore catalyst-free ambient pressure processing of ZnO nanowires with better property using simple and cost effective thermal evaporation technique.

The main objective of the present work includes:

1. Synthesis of good quality ZnO nanowires at ambient pressure using thermal evaporation and subsequent oxidation of Zn powder in the presence of oxygen flow.
2. Structural and optical characterization of the as-grown nanowires.

1.1 Outline of the thesis

This thesis work is presented in 5 chapters. The present chapter has covered the introduction of works that has been done on the area of the course, motivation to the present study, and the aim of this work.

In chapter 2, the necessary background information about the material (ZnO) will be presented. Some properties of ZnO including crystal and surface structure, electronic band structure, lattice vibrations and some important crystal defects in ZnO are discussed. This background information is given to lay the ground work for understanding the experimental data that will be presented in later chapters.

Chapter 3 presents the principle of thermal evaporation growth technique, which is used in this work for the synthesis of ZnO nanowires. Brief introduction of the growth mechanisms involved in the synthesis of nanostructures and description of the experimental procedure followed for the synthesis of ZnO nanowires is also presented in this section.

In chapter 4, the basic working principles of the characterization techniques used along with some background information for interpretation of the obtained results are introduced. The results of each characterization technique and detail discussion of the results are also presented in this section.

Finally, in chapter 5 conclusions for the present work, some recommendations and suggestions for the future works are presented.

Some fundamental properties of the alumina substrate are presented in appendix 1. Measurement results related to the alumina substrate, which are obtained during the structural and optical characterization of the as-grown ZnO sample, are also discussed in this section.

CHAPTER 2: ZnO fundamental properties and nanostructures

2.1 Crystal and surface structure

Zinc oxide crystallizes into three structures namely, Wurtzite, zinc-blend and rock-salt structure [13]. However, the zinc-blend ZnO structure can be stabilized only by epitaxial growth on suitable cubic substrates and the rock-salt structure is obtained by phase transformation at relatively high pressure. The stable structure of ZnO under ambient condition is the wurtzite hexagonal structure with a lattice constant of $a = 0.325\ nm$ and $c = 0.521\ nm$ [2]. Wurtzite structure belongs to the crystal symmetry of $P6_3mc\left(C_{6v}^4\right)$ space group and $6mm\,(C_{6v})$ point group [10].

The structure of ZnO is commonly represented as a number of alternating planes composed of tetrahedrally coordinated O^{2-} and Zn^{2+} ions, stacked alternatively along the c-axis as shown in figure 2.1 [14]. Locally, every atom is surrounded by four atoms of the other kind, which are arranged at the vertices of a tetrahedron. The O-Zn distance of nearest neighbours is 1.992 Å in the direction parallel to the c-axis of the hexagonal unit cell and 1.973 Å in the other three directions of the tetrahedral arrangement [15]. Furthermore, each ion also has twelve next-nearest neighbours of the same types of ions. The oppositely charged ions produce positively charged (0001)-Zn and negatively charged $(000\bar{1})$-O polar surfaces, resulting in dipole moment in the unit cell and spontaneous polarization along the c-axis. This induces divergence in surface energy along the different crystallographic direction.

As shown in figure 2.1b, the polarization vector due to the polar surfaces is perpendicular to the basal planes and such a polarization causes surface instabilities. In order to maintain the stability of a structure, the polar surfaces usually have facets or show substantial surface reconstruction. Nevertheless, it has been observed that the polar surfaces of $ZnO \pm (0001)$ are atomically flat, stable, and exclusive of reconstruction [1]. It is also observed that the (0001)-Zn surface is chemically active for the growth of nanostructures where as the $(000\bar{1})$-O surface is inert.

Wurtzite ZnO exhibits strong piezoelectric property. The origin of the piezoelectricity lies in its crystal structure, in which the oxygen atoms and zinc atoms are tetrahedrally bonded. In such non-centrosymmetric structure, the centre of positive charge and negative charge can be displaced due to external pressure induced distortion. This displacement results in local dipole moments and as a result macroscopic dipole moments appears over the whole crystal. It has been reported that among the other piezoelectric semiconductors, ZnO has the highest piezoelectric tensor which provides strong electromechanical coupling [2]. As a consequence, ZnO is a promising candidate for the fabrication of electro-mechanical coupled devices such as sensors, actuators, etc [1].

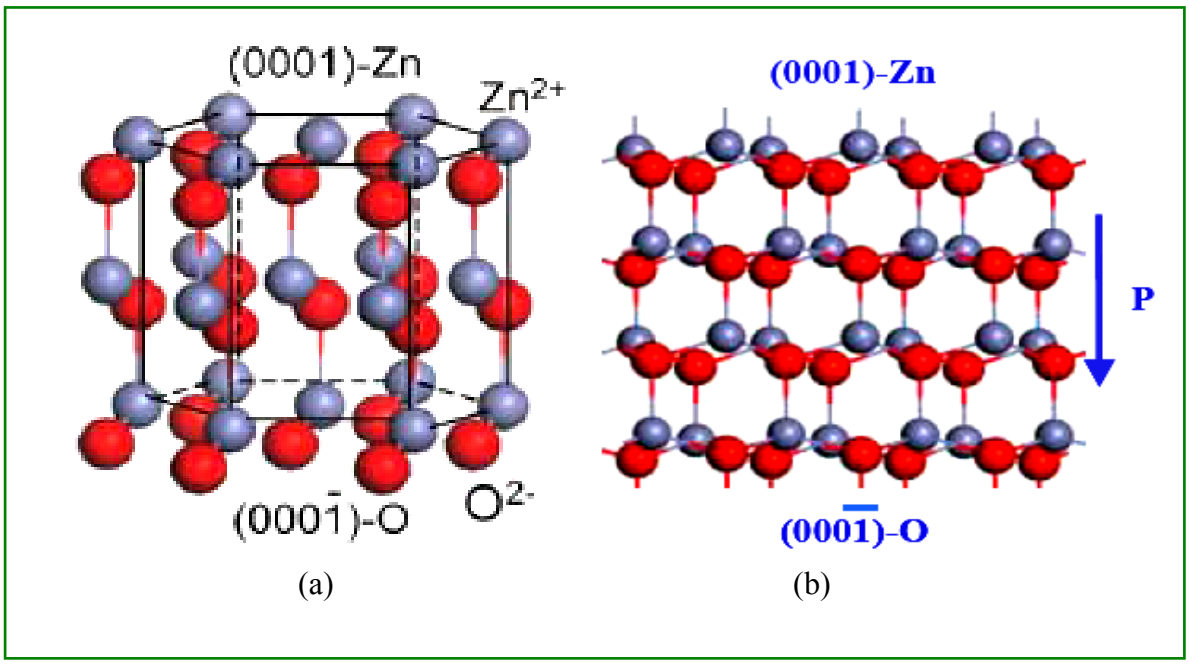

Figure 2.1-Crystal structure of ZnO (a) 3D representation and, (b) 2D representation [14].

From structural point of view, ZnO has three types and a total of 13 fast growth directions such as, $\langle 0001 \rangle$, $\langle 01\bar{1}0 \rangle$ and $\langle 2\bar{1}\bar{1}0 \rangle$ [1]. The non-polar $\{01\bar{1}0\}$ and $\{2\bar{1}\bar{1}0\}$ surfaces have lower energy than the $\{0001\}$ polar surfaces. The divergence in surface energy combined with the polar surfaces induce a phenomena which results in a wide range of ZnO nanostructures that can be grown by controlling the growth rates along the growth directions. One of the most profound factors determining the morphology involves the

relative surface activities of various growth facets under given conditions. According to the low energy principle, the [0001] plane is the fastest growing crystallographic plane compared to the other crystal facets. Moreover, the favoured crystallographic orientations of a crystal are driven by kinetics, and at a macroscopic level, different crystal planes have different kinetic parameter. Therefore, by controlling the growth conditions such as growth kinetics, local growth temperature, chemical composition of the source materials, the morphology of the product can be determined.

2.2 Lattice vibration modes

Atoms in a solid vibrate about their equilibrium position through interaction with their neighbours and the superposition of their vibrations forms wave of allowed wavelength and amplitude. This quantum of vibration is called phonons. Wurtzite structure ZnO has four atoms per unit cell and a total of 12 phonon modes corresponding to one longitudinal-acoustic (LA), two transverse-acoustic (TA), and nine optic phonons. A group theory analysis predicts that the optical phonon modes at the Γ point of the Brillouin zone have the symmetries of $A_1 + 2B_1 + E_1 + 2E_2$ [10]. Among these symmetries, the two E_2 phonon modes are only Raman active, where as A_1 and E_1 modes are both Raman and Infrared (IR) active. The B_1 modes are forbidden for both Raman and IR. Moreover, A_1 and E_1 modes are polar and their vibration polarizes the unit cell which results in the creation of a long-range electrostatic field. This in turn splits the polar modes into transverse optical (TO) and longitudinal optical (LO) components. For the lattice vibrations with A_1 and E_1 symmetries, the atoms move parallel and perpendicular to the c-axis, respectively. It has been identified that the high frequency E_2 mode (E_2(high)) is attributed to the vibration of the oxygen atoms where as the low frequency E_2 mode (E_2(low)) is associated with the vibration of heavy Zn sublattice [11,13].

A set of phonon mode frequencies for bulk ZnO, thin films and nanostructures have been measured using Raman spectroscopy (RS) and IR [16]. Table (2.1) shows a complete set of typical optical phonon modes of ZnO at the Γ point. The eigenenergies of the optical phonons at the center of the first Brillouin zone ($\vec{k} = 0$) ranges from 12.3 meV, which corresponds to the E_2(low) mode, to 72.5 meV for the E_1(LO) mode.

Table 2.1- Symmetries and typical eigenenergies of optical phonon modes of ZnO at the Γ point [16]. The accuracy or spread of the energies is $\pm 5cm^{-1}$ *or* $\pm 1meV$.

Symmetry	Wavenumber (cm^{-1})	Energy (eV)
$E_2(low)$ Γ_6	100	12.3
$B_1(low)$ Γ_3	240	29.7
$E_2(high)$ Γ_6	440	54.5
$B_1(high)$ Γ_3	540	66.9
$A_1(TO)$ Γ_1	380	47.1
$E_1(TO)$ Γ_5	410	50.8
$A_1(LO)$ Γ_1	577	71.5
$E_1(LO)$ Γ_5	590	72.5

Reports in literature [17] showed that Raman peaks of both polar and nonpolar phonon modes in ZnO nanostructures are shifted to lower frequency as compared to bulk ZnO. Moreover, the spectra from the nanostructures showed discrete spectrum of frequencies different from those of bulk phonons.

2.3 Energy band structure and optical properties of ZnO

2.3.1 Electronic band structure

For semiconductors, the energy of a single free carrier is described by the band structure $E(\vec{k})$, which is the function of quasi-momentum $\vec{k}$ that is determined by the periodic boundary conditions. Basically, the properties of the band structure are determined by the symmetry properties of the semiconductor crystal and the chemical binding of the constituting elements [18]. Thus, the band structure can be qualitatively understood by assuming the lattice periodic part of the Bloch functions are related to the atomic orbital of the constituting elements. This assumption is fulfilled for compounds with rather strong ionic contribution to the binding, including the II-VI compounds. Based on the atomic orbital model, the lowest conduction bands are mainly constituted by the lowest unoccupied s-levels that are generally from the cations where as the corresponding valence bands are formed by the highest occupied levels, which in most cases, are the p-levels of the anions.

The band structure of ZnO near the Γ point of the Brillouin zone is shown schematically in figure 2.2.The lowest conduction band arising from the 4s levels of Zn^{2+} or antibonding sp^3 hybrid has two fold degeneracy and Γ_7 symmetry. The upper most valence band originates from the 2p-levels of O^{2-} with some admixture of lower lying d-levels [16,19]. The valence band of the C_{6v} space group semiconductor is split by the crystal field of hexagonal wurtzite structure and the spin-orbit coupling into three degenerate valence bands usually labelled as A, B, and C from higher to lower energies [13]. The A, B, and C valence bands have symmetries of Γ_7, Γ_9, and Γ_7 respectively. The symmetries of the upper two valence bands of ZnO are reversed as compared to other II-VI semiconductors such as CdS that have symmetries in the order of Γ_9, Γ_7 and Γ_7 for A, B, and C bands respectively. This is from the fact that ZnO has negative spin-orbit coupling.

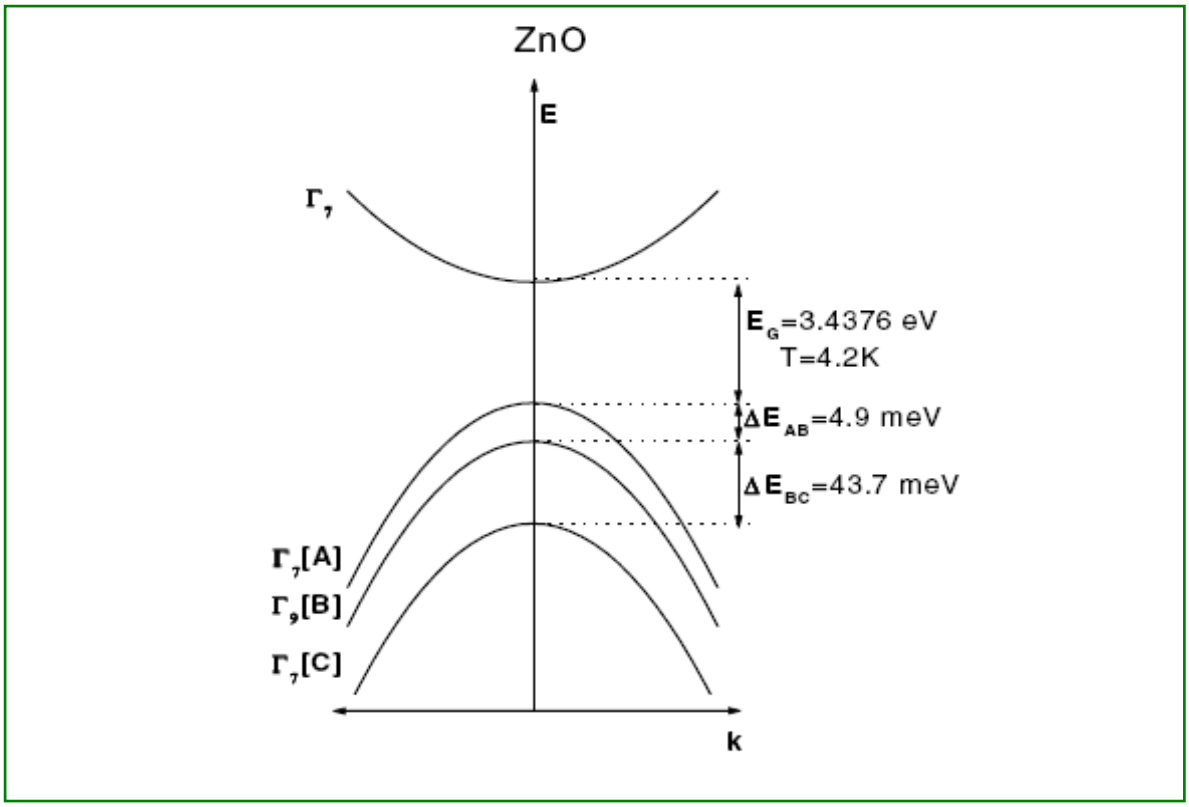

Figure 2.2-Schematic representation of the band structure of ZnO near the Γ point of the Brillouin zone [20].

The bandgap of a semiconductor changes with temperature. This change has been attributed to lattice expansion and electron-lattice interaction [21]. With increasing temperature the lattice constant and amplitude of oscillations of atoms around their equilibrium position increases. Moreover, the electron-lattice interactions are temperature dependent. For temperatures far below the Debye temperature (temperature of crystal's highest normal mode of vibration) the bandgap varies quadratically with temperature while for higher temperature the variation goes linearly. This temperature variation of the bandgap can be described by empirical Varshni equation as [22,23]:

$$E_g(T) = E_g(0) - \frac{\alpha T^2}{\beta + T} \quad \text{..... (2.1)}$$

where $E_g(0)$ is the bandgap energy at 0K, and α and β are constants to be determined from experimental data.

2.3.2 Free excitons in ZnO

At absolute zero temperature, an ideal semiconductor is in its ground state if there is no any excitation source. In the ground state, the bands below the top of valence band are totally filled with electrons and the conduction band is completely empty. If an electron is excited from the valence band to the conduction band by a photon of energy in the bandgap region (or by other excitation processes), the N electron system of the semiconductor is brought from the ground state to the excited state. The quantum of this elementary excitation is called "exciton" [19].

Another useful and simple model used to describe exciton is the effective mass model. In this view, exciton is considered as a pair of electron and hole that interacts through their coulomb field and influenced by the dielectric constant of the semiconductor. The interactions result in completely correlated motions of the paired electrons and holes and reduction of the total energy of the bound state relative to that of the unrelated free carrier states by an amount corresponding to the exciton binding energy. For the simple parabolic bands of a direct bandgap semiconductor, the relative motion of the electron and hole can be separated from the motion of the center of mass. Following this, the energy dispersion relation of exciton can be written as [19]:

$$E_{ex}(n,k) = E_g - \frac{R_y^*}{n^2} + \frac{\hbar^2 k^2}{2M} \quad \text{..... (2.2)}$$

Where E_g is the bandgap energy of the semiconductor; n = 1, 2, 3… is the principal quantum number, R_y^* is exciton binding energy, and $M = m_e + m_h \; and \; k = k_e + k_h$ are transitional mass and wave number of exciton, respectively.

The exciton binding energy (R_y^*) corresponding to the ground state (n=1) free exciton energy (E_{FX}) is given by:

$$R_y^* = 13.6 \frac{\mu}{\varepsilon^2}(eV) \quad \text{..... (2.3)}$$

With $\mu = \frac{m_e m_h}{m_e + m_h}$ the reduced mass of the electron and hole system and ε is the dielectric constant of the semiconductor.

Therefore, the excitonic energy levels near the Γ point with respect to the bottom of conduction band can be given by:

$$E_{ex} = \frac{R_y^*}{n^2} \quad \text{..... (2.4)}$$

This suggests that the exciton states can exist in a series of excited states in similar way as excited states of hydrogen like atomic systems, with ionization limit corresponding to the bottom of conduction band as shown in figure 2.3.

The corresponding exciton Bohr radius is also given by:

$$a_x = \frac{\varepsilon \hbar^2}{\mu e^2} \quad \text{..... ..... (2.5)}$$

As mentioned earlier, the valence band in ZnO splits into three doubly degenerate subbands labelled as Γ_9, Γ_7 and Γ_7 due to the hexagonal crystal field splitting and spin-orbit coupling interactions. Corresponding to these subbands, three types of holes can be distinguished by different effective masses. Consequently, ZnO has three series of excitons which are formed due to the coulomb interactions of electrons in the Γ_7-conduction band with holes in the three subbands. These excitons are usually called as $A(\Gamma_7 \rightarrow \Gamma_7)$, $B(\Gamma_7 \rightarrow \Gamma_9)$ and $C(\Gamma_7 \rightarrow \Gamma_7)$ excitons [13].

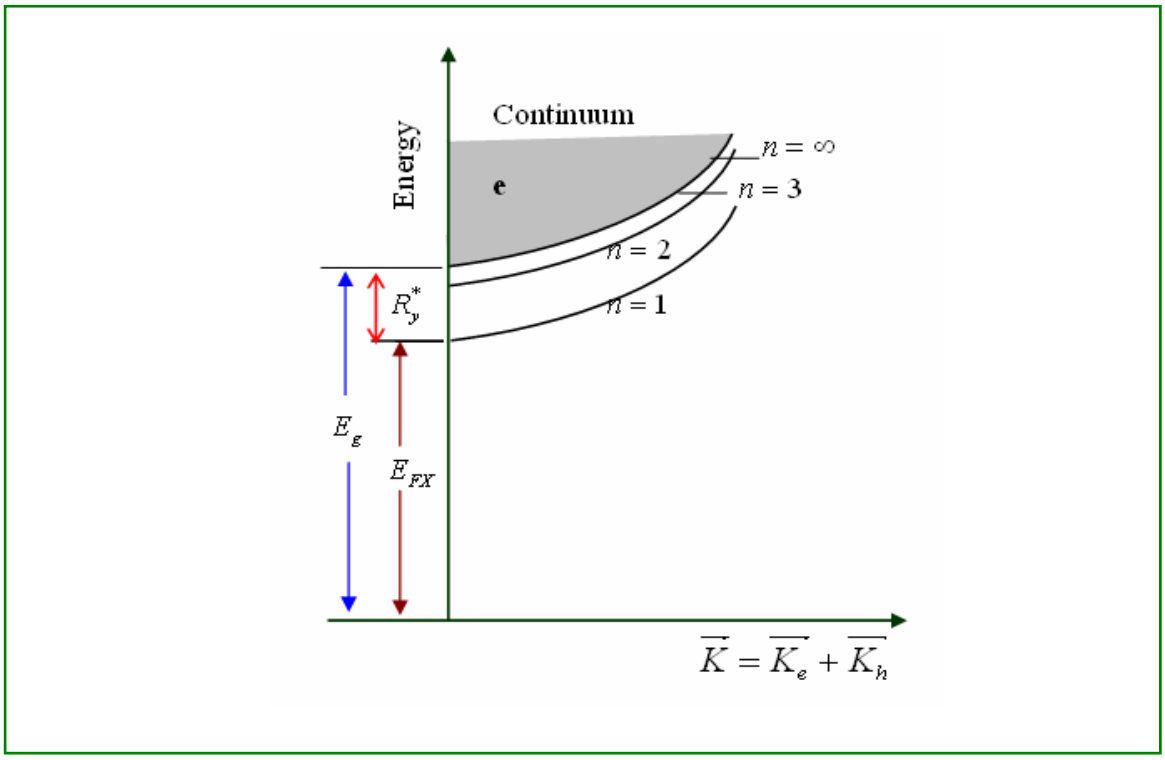

Figure 2.3-Schematic energy levels of an exciton for direct bandgap semiconductor near the Γ point, adapted from [16].

The splitting of the valence band and the corresponding excitonic properties can be experimentally determined from the low temperature photoluminescence (PL), photoreflectance (PR), absorption, and reflection measurements [13]. In terms of the irreducible representations in C_{6v} point group of the corresponding bands and the electrical field vector $\left(\vec{E}\right)$ of the light beam with respect to the optic axis $(\vec{c}-axis)$, the following selection rules has been identified for the three excitons [13]:

1. For σ polarization $\left(\vec{E}\perp\vec{c}\ and\ \vec{k}\perp\vec{c}\right)$, transitions are allowed for all the three excitons however, the C exciton is quite weak.
2. For π polarization $\left(\vec{E}//\vec{c}\ and\ \vec{k}\perp\vec{c}\right)$, the C exciton is strongly allowed where as the B exciton is weakly observable. Exciton A is forbidden in this geometry.
3. For α polarization $\left(\vec{E}//\vec{c}\ and\ \vec{k}//\vec{c}\right)$, all three transitions are clearly observable.

Based on this selection rules, Thomas first investigated the fundamental free exciton spectrum of ZnO crystal by using reflection and absorption measurements in 1960 [13]. The measurement was performed over a range of temperature from 4.2K to 300K. He

identified three excitonic series associated with the three valence subbands using different geometries of light polarization with respect to the optic axis. A typical reflection spectrum is shown in figure 2.4.

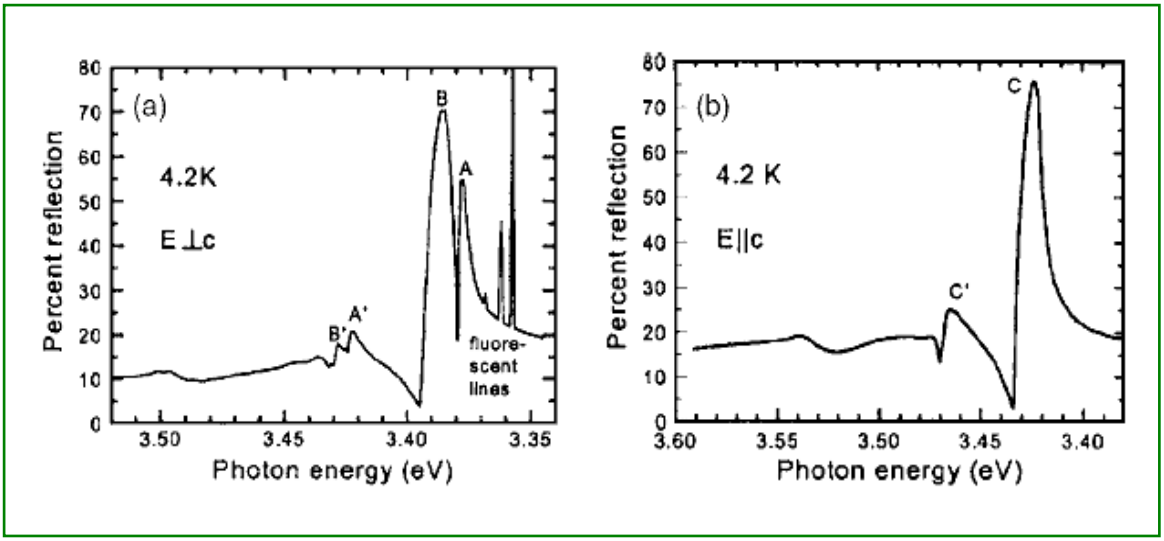

Figure 2.4-Reflectivity spectra of ZnO at 4.2K for $\vec{E} \perp \vec{c}$ *and* $\vec{E} // \vec{c}$ [13].

The low temperature PL has been also widely used to investigate the excitonic emissions of ZnO and hence for the determination of exciton binding energies, exciton Bohr radii, dielectric constant, spin-orbit coupling and crystal field parameters. Teke *et al.* has taken the PL spectrum of ZnO single crystal in the $\vec{E} \perp \vec{c}$ polarization geometry at 10K. In the spectra, the A free exciton and its first excited state transitions are observed. Figure 2.5 shows the typical spectra in the fundamental excitonic region (detail description can be found in reference [13]). Using the energy separation of ground and excited state peak position and the hydrogen model of exciton, the exciton binding energy and the bandgap energy was predicted as 60 meV and 3.4371 eV, respectively.

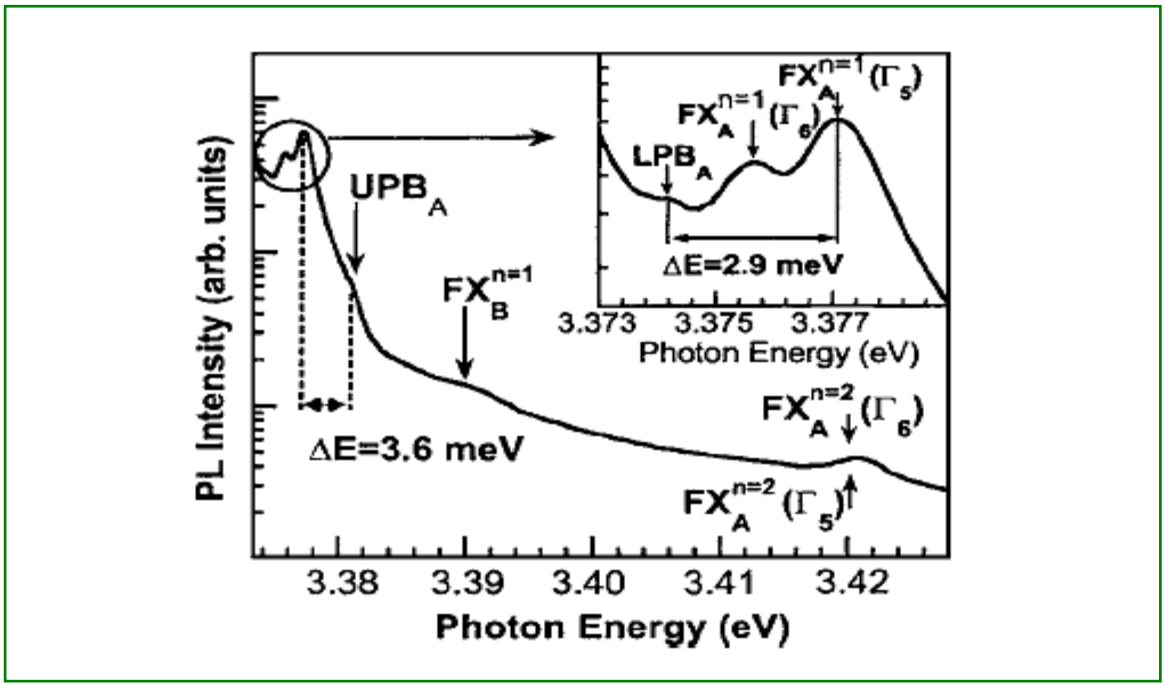

Figure 2.5-Free exciton fine-structure region of the 10K PL spectrum for ZnO [13].

2.3.3 Electronic energy levels of native defects in ZnO

Under the common physical preparation condition, excess zinc ion is usually found in ZnO. Due to this zinc excess, ZnO is non-stoichiometric compound with relatively open structure and an n- type semiconductor. In literature, point defects such as Zn interstitial, Zn vacancy and oxygen vacancy in ZnO are referred to be the native lattice defects of the material [5,24]. Zn interstitials and oxygen vacancies are expected to act as donors, and these defects have frequently been invoked as source of high carrier concentration. However, Zinc interstitials have high formation energies and low diffusion barriers, and therefore, unlikely to be incorporated into the stable ZnO structure [13]. As for oxygen vacancies, they have the lowest formation energies though oxygen is considered to be a deep rather than shallow donor in ZnO structures. Oxygen vacancies can theoretically take three different charge states: the V_O^x state which has captured two electrons and is neutral, the singly ionized V_O^+ state, and the V_O^{++} state which did not trap any electron and is doubly positive charged.

Zinc interstitials can also take Zn_i^x, Zn_i^+, *and* Zn_i^{++}. However, the valence states of zinc interstitials often depends on the temperature and process condition. Another defect in ZnO is the zinc vacancy, which is represented as V_{Zn}^x, V_{Zn}^- and V_{Zn}^{2-}, respectively for neutral, singly charged and double charged zinc vacancy, occupying the acceptor energy levels. The location of the energy levels for native defects in ZnO has been estimated based on numerous studies of its electrical and optical properties. These typical energy levels are shown schematically in figure 2.6. The locations of the energy levels are given with respect to the bottom of the conduction band or to the top of valence band. In the figure, the full arrows indicate non-radiative transition where as the half arrows stand for radiative transition.

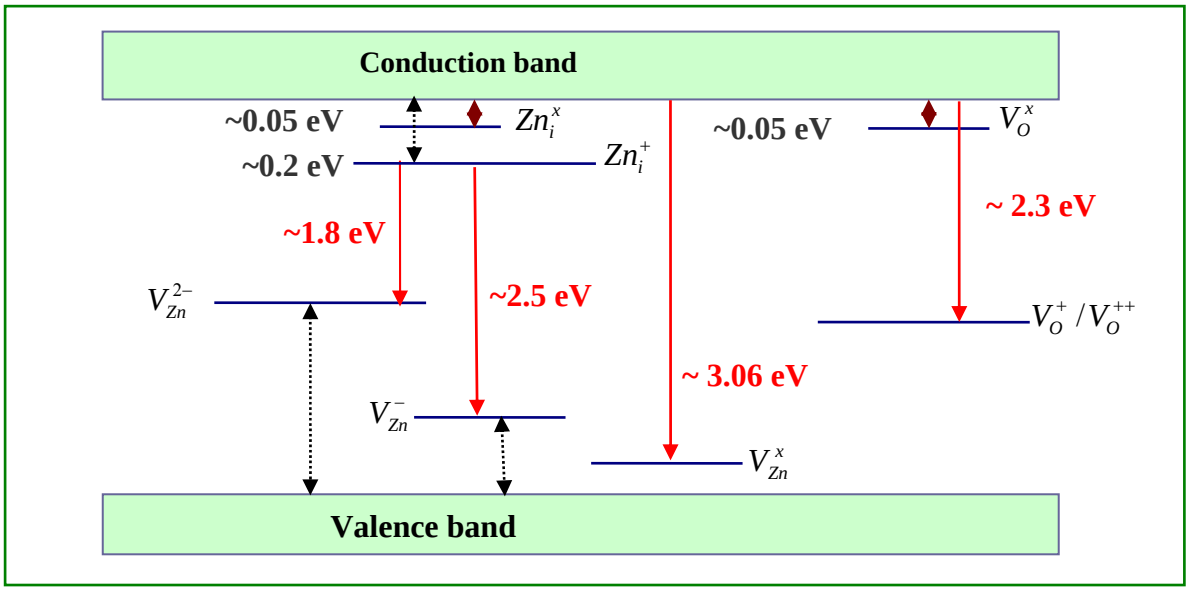

Figure 2.6-Electronic energy levels of native defects in ZnO, adapted from [5,24].

2.4 Nanostructures of ZnO

ZnO nanostructures have been extensively studied due to their tremendous potentials as building blocks for fabricating nanometre-scaled devices as well as for understanding fundamental phenomena at low dimension. So far, various types of ZnO nanostructures, including nanorods [10,11], nanowires [3,6], nanoneedles, nanostars [9], nanobelts, nanobows, nanosprings, nanohelixes, nanocages [25,26], flower-shaped ZnO

nanostructures and so on have been synthesized using various fabrication techniques under specific conditions. Some typical nanostructures are shown in figure 2.7.

The growth of various morphologies of the nanostructures mainly relies on the divergence in growth kinetics along the preferred growth directions and the polar surface induced phenomena. Different facets of a crystal have different energy. Among the fast growth facets of ZnO, $\langle 2\bar{1}\bar{1}0 \rangle$ and $\langle 01\bar{1}0 \rangle$ facets have lower surface energy than the $\langle 0001 \rangle$ facets. Therefore, the $\langle 0001 \rangle$ facet is thermodynamically favourable for growth, and hence leads to growth along c-axis. As a consequence, one-dimensional structures such as, nanowires, nanorods, and nanobelts can be obtained under different processing condition. In a similar manner, the formation of other nanostructures such as nanorings and nanohelixes can be understood by considering the nature of polar surfaces. For instance, if the surface charges are uncompensated during growth of nanobelts, the spontaneous polarization induces electrostatic energy due to the dipole moment. Thus, the nanobelts can roll up forming a circular ring which would minimize or neutralize the overall dipole moment and hence reduce electrostatic energy. This bending of nanobelts on the other hand produces elastic energy. Therefore, thermodynamically stable shape of the nanobelts is determined by the minimization of the total electrostatic and elastic energy.

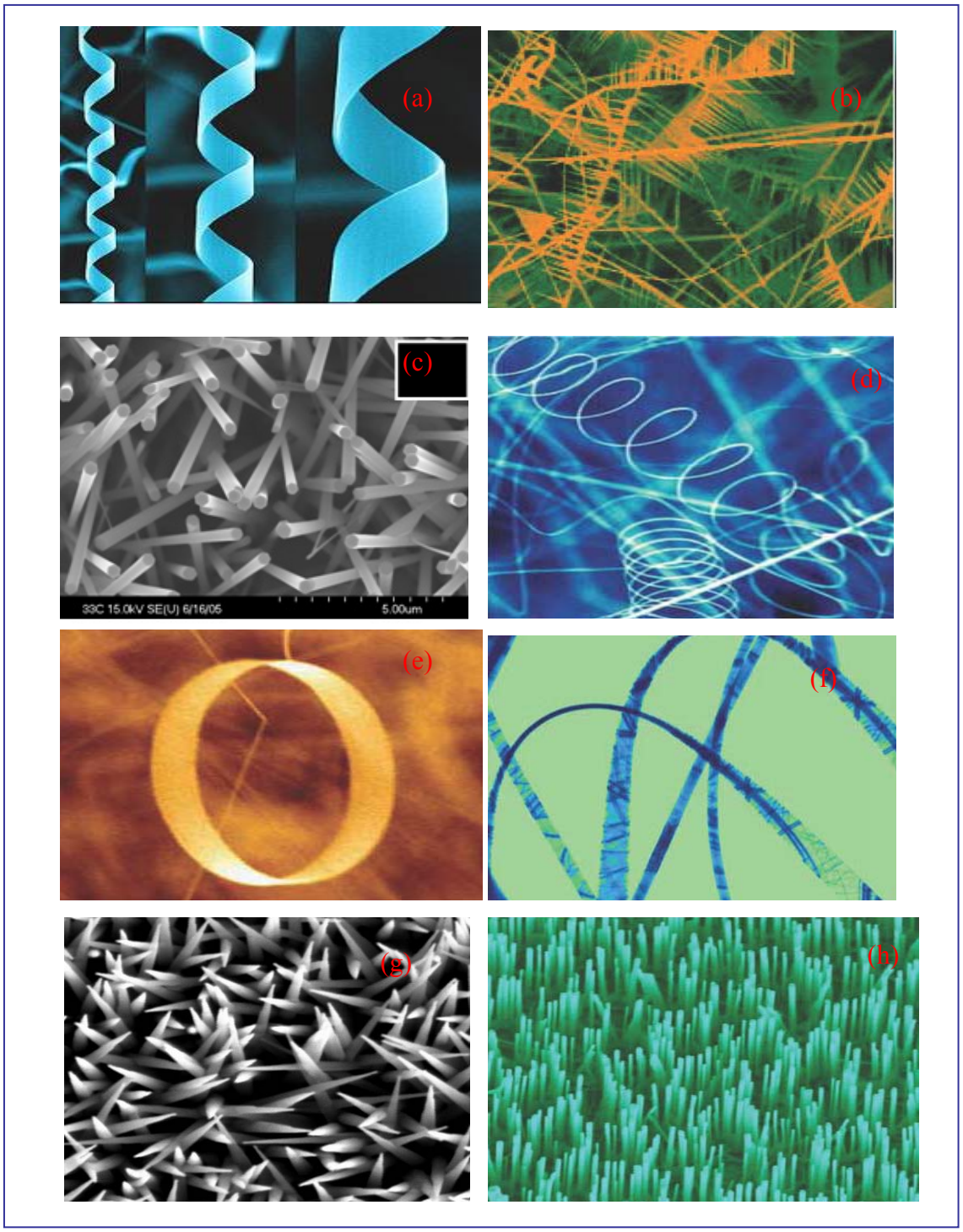

Figure 2.7-Collection of ZnO nanostructures. (a) nanohelix, (b) nanocomb, (c) nanorod, (d) nanospring, (e) nanoring, (f) nanobelt, (g) needle-shaped nanowire, (h) nanowire, [10,14].

CHAPTER 3: Thermal evaporation growth of ZnO nanowires

3.1 Introduction

The thermal evaporation technique is based on a simple process in which the source material in the condensed or powder form are first vaporised at an elevated temperature and the resulting material in vapour phase then condenses under certain conditions (temperature, pressure, atmosphere, substrate, etc.) to form the desired product. The typical heating sources used include electron-beam, radio frequency (RF) inductive and resistive heating.

In electron-beam evaporation, an electron source is aimed at the source material causing localized heating. The RF induction uses an AC power supply to produce an alternating current through an induction coil. This alternating current generates a magnetic field in the coil. When the source material is placed inside the coil, the magnetic field induces current within the source material providing localized heat. Finally, resistive heating provides heat by sending a high current source through a resistive coil, such as tungsten, and is a non-localized heat source and therefore commonly used for furnace applications. Among the three heating sources the resistive sources have been widely used to produce thin films as well as various nanostructures of ZnO with different shapes, size and orientations [1,7,10,24].

In this thesis work, thermal evaporation growth of ZnO nanowires was performed in a horizontal tube furnace which uses resistive heating. The detailed description of the synthesis setup and procedures will be given in later sections. Prior to that, it is important to make some general considerations about the common growth mechanisms involving vapour condensation.

3.2 Growth mechanisms

In the past years, one-dimensional nanostructures have been developed and synthesized by different techniques. These fabrication techniques can be categorized into four groups namely, spontaneous growth, template based synthesis, electrospinning and lithography [27]. Among these techniques the first three are considered as bottom-up approach where as lithography is a top-down technique. Spontaneous growth commonly results in the formation of single crystal nanowires or nanorods along a preferential crystal growth

direction depending on the crystal structures and surface properties of the nanowire materials. On the contrary, template based synthesis mostly produces polycrystalline or amorphous products. The thermal evaporation technique used for the synthesis of ZnO nanowires in this thesis work is categorized under spontaneous growth; hence attention will be given to this growth method. Further information on the other techniques can be obtained in reference [27].

The driving force for spontaneous growth is the reduction of Gibbs free energy, which can be realized by phase transformation, chemical reaction, or stress release. For the formation of nanowires or nanorods, anisotropic growth is required. Moreover, uniformly sized nanowires (uniform diameter along the longitudinal direction) can be obtained when crystal growth proceeds only along one direction. Crystal growth by thermal evaporation can be explained by two distinct features of vapour condensation and solidification. Either the vapor first condenses into a liquid which then condenses into solid or the vapor bypasses the liquid state and transforms directly to the solid state. Accordingly, two mechanisms of growth for one-dimension structures have been proposed. The first mechanism is the vapor-liquid-solid (VLS) where as the second mechanism is vapor-solid (VS) growth [21]. The detail description of VS growth, which is inline with the present work, and brief introduction of VLS method, is presented in the following subsections.

3.2.1 Vapour-solid (VS) growth

The fundamental growth of one-dimensional nanostructures is historically based on early work on growth of whiskers. As defined in [27,28], a whisker is a single-crystal eruption from a surface of a deposited metal film. Whiskers typically have 5 microns diameter with lengths of 1-500 microns. Based on early works on the growth of whiskers, several mechanisms have been proposed for the origin of anisotropic growth which leads to the formation of one-dimensional nanostructures. These mechanisms include: anisotropy in growth rate of different facets of crystal, presence of imperfections in specific crystal directions such as, screw dislocation, and preferential accumulation of impurities on specific facets.

Dislocation theories describing the root growth of whiskers have been proposed by different authors in the 1950's [25]. However, Sears was the first to explain axial screw

dislocation induced anisotropic growth of whiskers [27]. For whiskers (nanowires) grown by simple evaporation condensation under low supersaturation, he observed that the diameter of the nanowires remained constant throughout the axial growth. On this base, he proposed that for sufficiently low vapour supersaturation, growth could occur at the tip of whiskers rather than at base. Obviously, the growth species simultaneously condense at the tip as well as the side walls. Therefore, under the assumption that nucleation and growth occur only at the growth front, condensed species on the walls must either migrate to the tip of the whisker or desorbs from its surface. As diffusion limited process, Sears suggested that the growth rate increases exponentially for whisker length less than the mean diffusion distance of the desorbed species. In comparison, if the whisker length is greater than the mean diffusion distance, the rate would be linear since the species would arrive at the tip at constant rate with dependence on the partial vapour pressure within the environment. More generally, if h is the instantaneous length at time t and h_0 is the length at $t = 0$, the exponential growth is given by [28]:

$$h = h_0 \exp\left(\frac{nt}{g}\right) \quad \text{..... (3.1)}$$

where n is the number of species condensing onto the surface per unit area per second and g is the geometrical constant.

Expanding on the Sears' concept, Blakely and Jackson [28, and references therein] solved for two-dimensional nucleation probability (P_n) on the surface of nanowires as:

$$P_n = B \exp\left(\frac{-\pi\sigma^2}{k^2 T^2 \ln\alpha}\right) \quad \text{..... (3.2)}$$

where B is a constant, σ the surface energy of the solid nanowire, k is the Boltzmann constant, T is absolute temperature, and α is a measure of supersaturation defined as the ratio of actual vapour pressure, P and equilibrium vapour pressure P_0 at temperature T $(\alpha = \frac{P}{P_0})$.

From equation (3.2), one can clearly infer that lower surface energies correspond to greater two-dimensional nucleation probability. On the other hand, low energy surfaces have smaller sticking coefficient as compared to the higher energy surface counterparts. Consequently, adsorbed species will have a higher probability of desorption on this low

energy surfaces. Therefore, balance between these two distinct effects is essential for the formation of low energy crystal planes that commonly enclose whiskers and one-dimensional nanostructures. As a result of this investigation, the growth of whiskers as well as one-dimensional nanostructures is identified as kinetically-driven anisotropic crystallization processes that are heavily dependent on temperature and supersaturation [27,28]. Lower temperature and lower supersaturation are required for nucleation and growth of nanowire-like structures. However, it should be noted that the concentration (saturation) is ideally higher than the equilibrium concentration of the growth surface [27]. On the contrary, higher temperature and larger supersaturation facilitate two-dimensional nucleation resulting in the formation of films. In summary, temperature and supersaturation are the two dominant factors during VS growth and provide the ability to control morphology of the deposited product.

Based on the aforementioned criteria, the VS growth process can be considered as self-catalyzed. The growth of ZnO nanowires by simple thermal evaporation via VS mechanism has been reported in literature. Zhang *et al*. [29] synthesized well aligned ZnO nanowires on ZnO thin film, which is grown on sapphire using pulsed laser deposition, at temperature of ~750ºC using Zinc powder. Zhang found that temperature was the critical experimental parameter for the formation of different morphologies of ZnO nanostructures. In addition, it has been reported by several research groups [5-8] that the type of growth is also controlled by the pressure, oxygen availability, and gas flow, which all affect one another and create a specific vapour environment which leads to the growth of various nanostructures. Therefore, a general understanding of the conditions that control the growth and underlying growth mechanism is crucial for achieving reproducibility in the growth of nanostructures.

3.2.2 Vapor-liquid-solid (VLS) growth

In the VLS growth, a second phase material, commonly referred to as either impurity or catalyst, is purposely introduced to direct and confine the crystal growth onto a specific orientation and within a confined area. A catalyst forms a liquid droplet by itself or by alloying with growth material during the growth, which acts as trap of growth species. Enrich growth species in the catalyst droplet subsequently precipitates at the growth surface resulting in the one-dimensional growth. An important identification of the VLS

mechanism is that it leaves residues from the impurities at the tip of the grown structures. ZnO nanowires grown by this mechanism has been reported by several authors. Yang *et al.* [11] presented controlled growth of ZnO nanowires on Au-coated single crystalline silicon and sapphire substrates using chemical vapour transport and condensation (CVTC) method. ZnO powder and graphite flakes were used as source material and it has been observed that the absence of graphite in the starting material produces essentially nothing on the Au-coated substrates, which indicates the importance of Zn vapour generated by the carbothermal reduction of ZnO. Banerjee *et al*. [6], also succeeded in producing large-quantity free standing ZnO nanowires via thermal evaporation of ZnO powder and graphite powder in tube furnace at high temperature and lower pressure (1-2 Torr). The graphite flakes were found to be the key ingredient for the large quantity growth and can be easily removed by oxidation of the as-made samples at different temperature for 1-3h in oxygen flow.

3.3 Synthesis setup

The thermal evaporation process used for the synthesis of ZnO nanowires was carried out in an alumina tube (150 cm length and 70 mm inner diameter) which is placed in a horizontal tube furnace. The system mainly consists of a horizontal tube furnace, alumina tube, gas supply and control systems, set of thermocouples, and a computer with seven channel temperature data logger software. The schematic illustration of the setup is shown in figure 3.1.

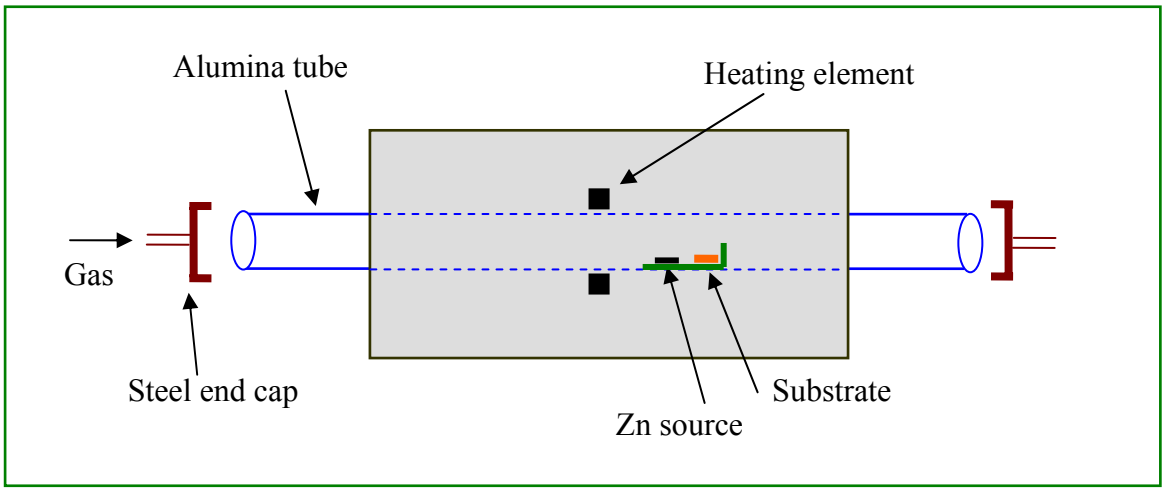

Figure 3.1-Schematic illustration of the general experimental setup for the growth of ZnO nanowires.

The furnace used was a three zone (model ETF 70/12-3, Entech) high temperature tube furnace which consists of a series of resistive heating elements in three regions with respective temperature controller units. The heating elements are serially combined forming temperature gradient within the three zones of the tube furnace in such a way that the temperature decreases outwardly from centre of the furnace. However, in this particular work, the heating elements of the two side zones were disconnected on purpose and only the master controller unit at the centre was used. For further illustration, the picture of the furnace is shown in figure 3.2.

The alumina tube was equipped with adjustable steel end caps on both ends to enable the experiments in controlled gas atmospheres. Furthermore, the steel end cap on one end of the tube was specially designed in such a way to hold a set of thermocouples which were used to monitor the temperature in different regions of the furnace through seven channel temperature data logger installed to a computer.

Figure 3.2-Horizontal tube furnace used for the synthesis of ZnO nanowires.

3.4 Experimental procedure

As stated earlier, synthesis of the nanowires was carried out by vapour-solid deposition technique and the process is initiated by thermal evaporation.

The first step of the synthesis process was to clean the alumina tube. The tube was cleaned in a succession of ethanol (96%) and water. After cleaning, the tube was then dried in air and covered with a thin cotton-like cloth (on its ends) to prevent contamination during loading into the furnace. Once the tube was inside the furnace, a series of thermocouples were inserted into the tube furnace for temperature calibration. The purpose of calibration was to observe the temperature profile within the alumina tube. For illustration the profile along the tube, when the temperature inside alumina tube at the centre of the furnace was stabilized at 850ºC, is shown in figure 3.3. While measuring this profile, the left end of the tube is sealed and the right end is kept open to air. It is clearly observed that the temperature gradient between two points increases as one move from the centre to the end of alumina tube. This increases the freedom of choosing any temperature gradient for the synthesis of nanowire growth. Moreover, this curve can be used to interpolate or extrapolate to some extent the temperature at any point during the synthesis process.

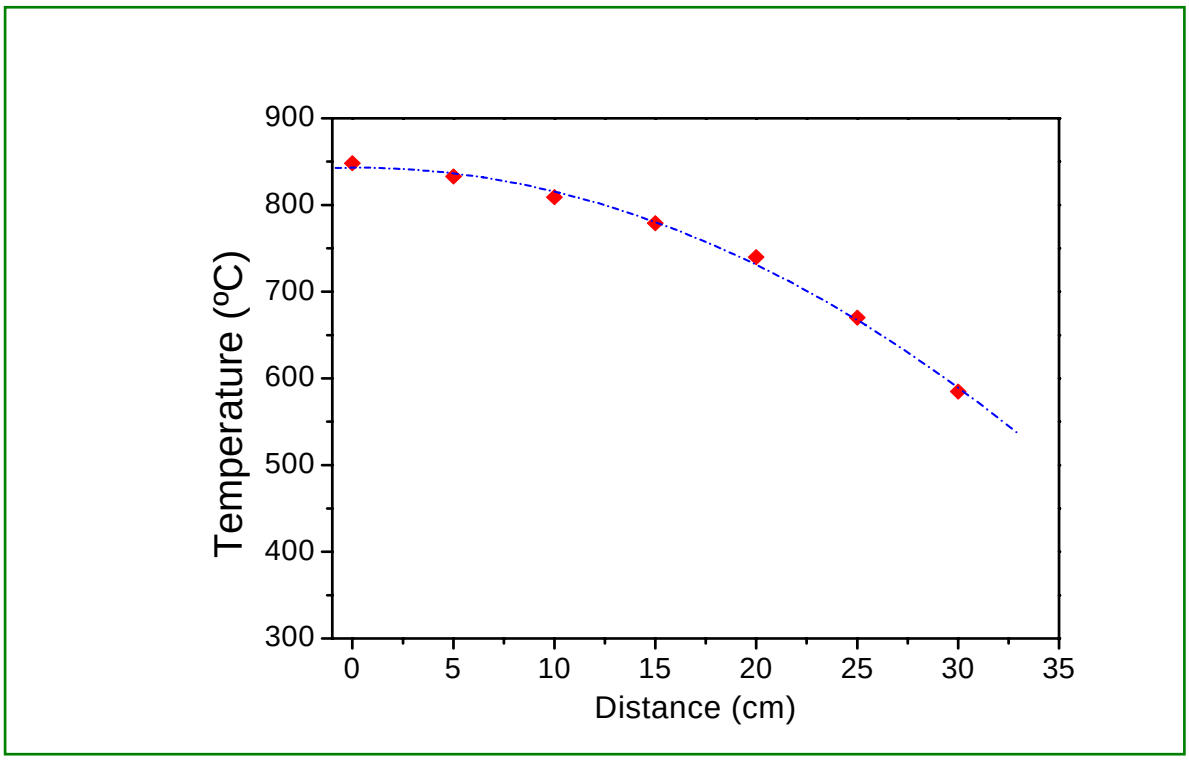

Figure 3.3-Temperature profile along the alumina tube, the distance is between the centre of the furnace and given position along the tube to the right end.

After calibration of the furnace temperature, the synthesis was carried out as follows. Zinc powder (commercial, 99% purity) was spread in a modified (one end-open, 7 cm length) alumina boat near its open-end edge as shown in figure 3.4. In the same boat, an alumina substrate with sprinkled zinc powder on its surface was placed downstream adjacent to the source material at the corner edge of the closed side of the boat. The boat was then placed at distance of 25-30 cm from the centre of the furnace, with its open end facing the centre of the tube. Once the boat is placed at the desired position, the left end of the tube was covered using the steel end cap and sealed while the right end was kept open to air throughout the whole process in order to optimize the temperature gradient between the source material and substrate during the process. Nitrogen gas at flow rate of 500 sccm (standard cubic centimetres per minute) was introduced from left end of the furnace during the whole synthesis process. When the temperature at the middle of boat was raised to 420ºC, oxygen gas was supplied at flow rate of 90 sccm and maintained until the end of growth process. After the furnace temperature (at center) is stabilized at desired temperature of 850ºC, a sharp temperature gradient from ~672ºC at the middle of boat to ~618ºC at the substrate position (over a distance of 3-3.5 cm) is observed. This temperature was maintained for 60 minutes and then the furnace is naturally cooled down to room temperature. The surface of the zinc source on the boat showed gradual colour change along the boat length from white on upstream to dark grey on the substrate side and whitish gray colour is observed on the substrate surface. The as-grown sample was then characterized by various structural and optical characterization techniques.

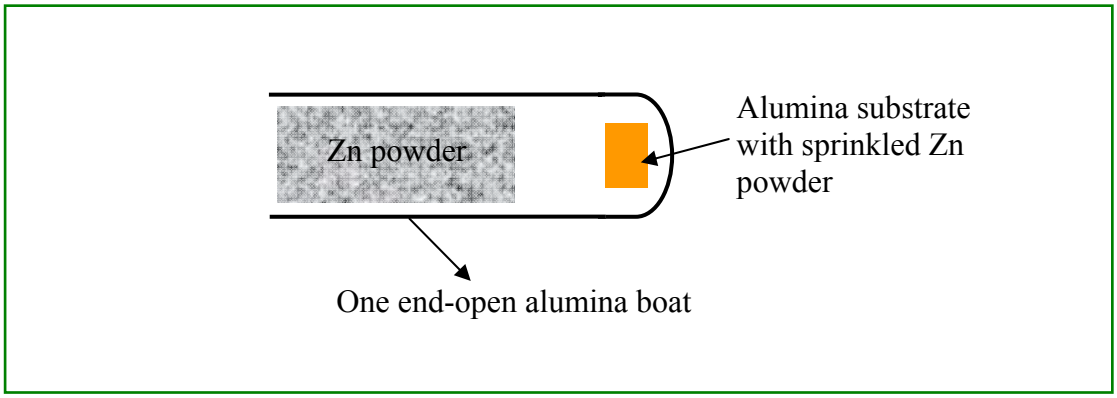

Figure 3.4-Schematic representation of the substrate and source material placement on one end-open alumina boat.

CHAPTER 4: Characterization of ZnO nanowires

A variety of characterization techniques were used to analyse the morphology, structural and optical properties of the as-synthesised ZnO nanowires. These include scanning electron microscopy (SEM), X-ray diffraction (XRD), Raman spectroscopy (RS), and photoluminescence (PL) spectroscopy. This section presents brief description of each technique used followed by the results and discussion. Some related basic theories and literature reviews are also included in order to use for interpretation of the experimental data.

4.1 Morphological and structural characterization

4.1.1 Scanning electron microscopy

In a typical SEM, a source of electron focused into a beam is scanned over the surface of a specimen by deflection coil. As the electrons strike and penetrate the surface, a number of interactions occur that result in the emission of electrons and photons from the sample. The scanning electron microscopy uses emitted electrons to produce the image of the sample. In this thesis, the morphology of as-grown ZnO nanowires was investigated using field-emission scanning electron microscopy (ZEISS 1540XB SEM).

4.1.1.1 Results and discussion

A typical SEM image of the as-grown ZnO nanowires is shown in figure 4.1. As it can be seen from the SEM image, the surface of the substrate is not homogenously covered with the nanostructures. Moreover, the observed sample shows a unique morphology consisting of bulk seed-like structure at the base with outwardly growing nanowires on their surfaces. This morphology can be explained with reference to the growth condition. Up on heating the furnace to the growth temperature, Zn vapour is continuously generated from the source material in the boat as well as the sprinkled powder on the substrate. Moreover, rate of generation of vapour increases with temperature. These results in high vapour supersaturation which leads to bulk growth observed as seed-like structure at the base. After the seed-like structure is formed the vapour comes only from source material through a carrier nitrogen gas. Moreover, after growth temperature is attained, the vapour is

generated from the source material at constant rate resulting in lower supersaturation. This reduction of supersaturation combined with anisotropy in surface energy of the crystal leads to the initiation and growth of nanowires on the seeds. Hence, the seed has acted as a catalyst for the upcoming vapor to grow in a certain crystallographic direction. A similar phenomenon has been reported in literature for the growth of ZnO nanowires after the formation of ZnO thin films on silicon substrate [10].

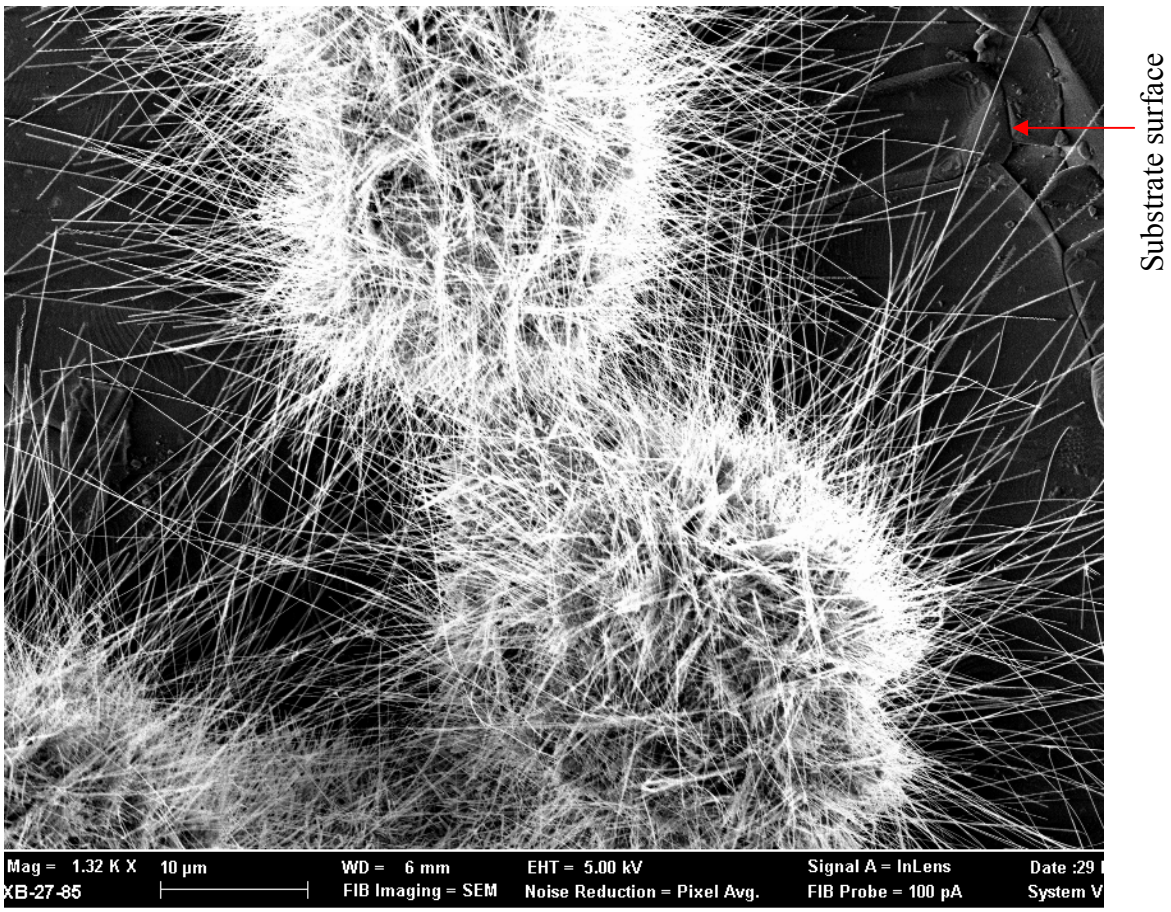

Figure 4.1-Typical SEM image of ZnO nanowires grown on alumina substrate.

High resolution SEM image of nanowires on a single seed is shown in figure 4.2. The nanowires have diameter ranging from $70-80\,nm$ and length of $10-15\,\mu m$. This shows relatively high aspect ratio of the nanowires. Moreover, as it can be seen from the SEM image, no any metal particles are observed at the tip of the nanowires, which is expected in the VLS growth mechanism. From this observation, and of course as the growth is carried

out without the use of metal catalyst, we can predict that the grown nanowires do not follow the VLS mechanism rather the VS mechanism. The SEM image also shows high density of nanowires on each seed which is an indication to the high yield of nanowires. Figure 4.3 shows high magnification of the nanowires. The nanowires show considerably uniform surfaces with less surface defects. However, the curvature observed on some of the wires could be due to electron charge effects or shaking of the sample while taking the measurement.

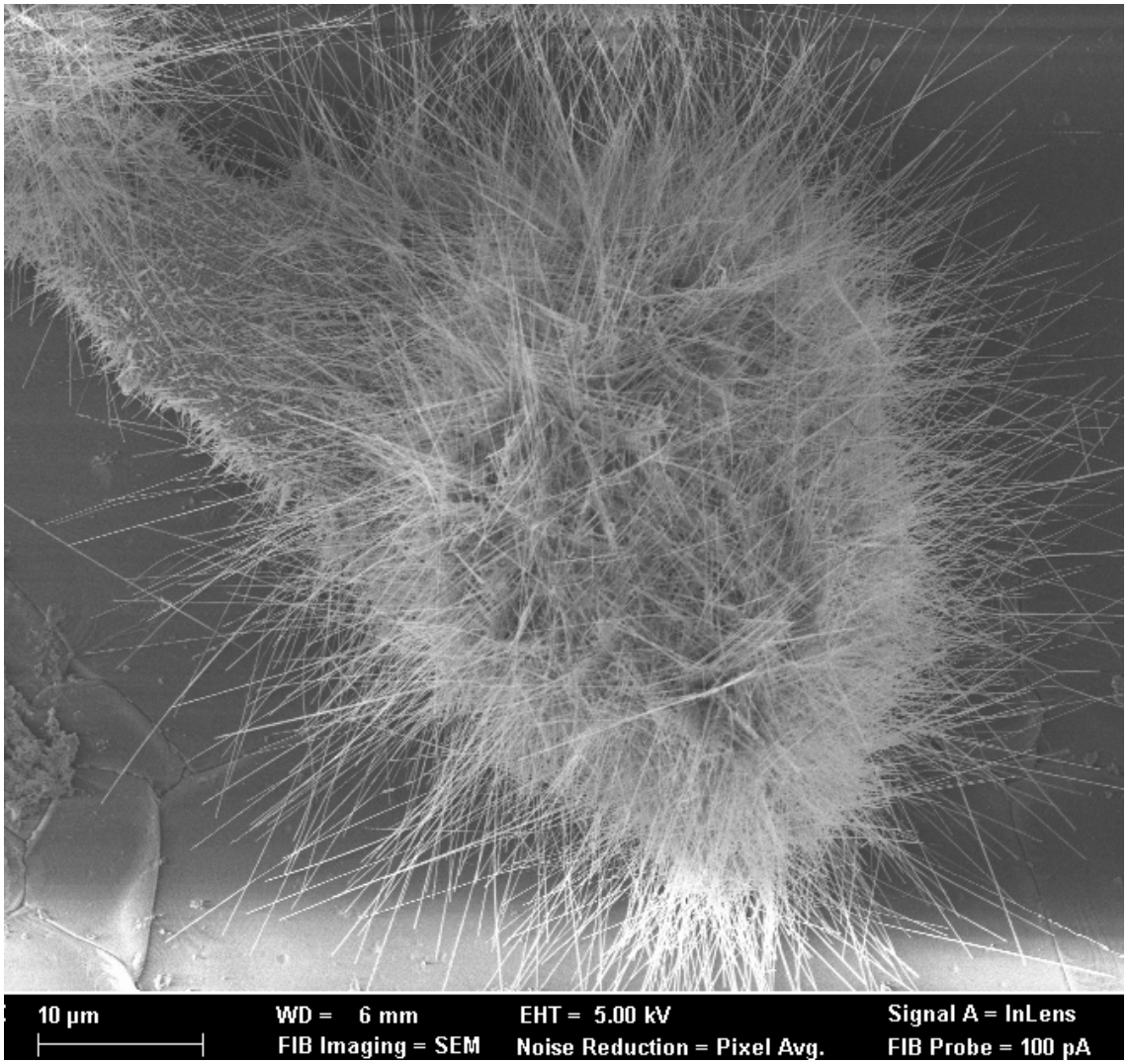

Figure 4.2-Typical SEM image showing the distribution of ZnO nanowires on a single seed.

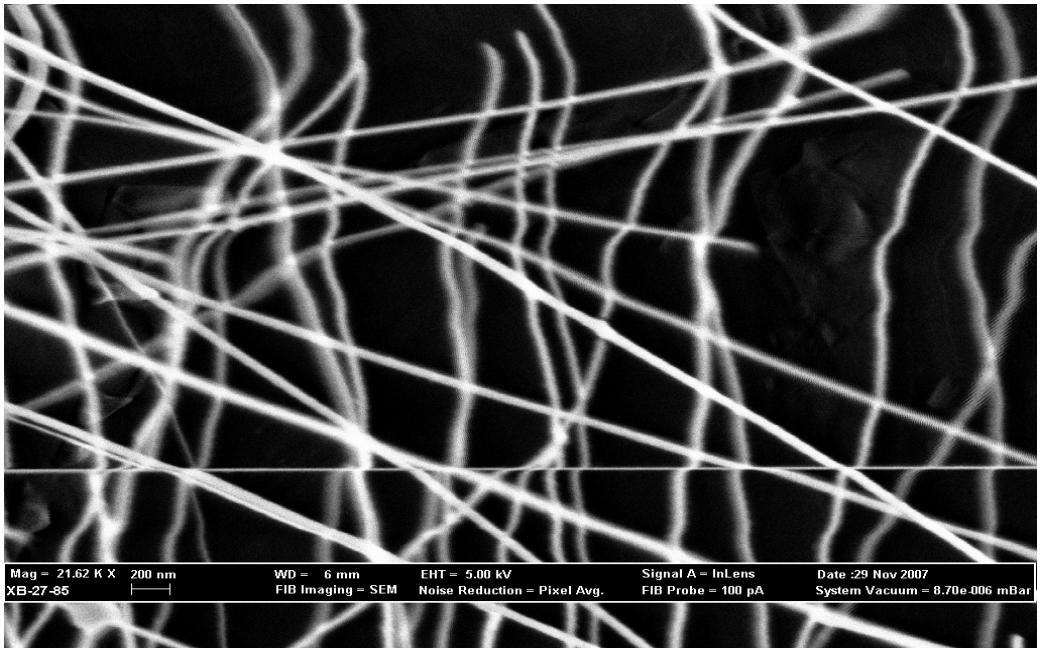

Figure 4.3-High magnification SEM image of ZnO nanowires.

The growth of ZnO nanostructures by vapour deposition in a tube furnace is typically affected by several factors including temperatures of the source material and the substrate, the distance between the source and substrate, the gas flow rate, deposition pressure, tube diameter and starting materials [5,9,12]. These factors affect the growth in deferent ways. For instance, the substrate temperature can determine the length of surface diffusion of the adsorbed species as well as the amount of vapour required for condensation. Similarly, the deposition pressure affects the supersaturation level of the vapour, and this determines the type of growth to occur as bulk or nanostructure [12,27]. In this regard, the ambient pressure processing has the advantage of excluding effect of deposition pressure. The distance between the substrate and source material also affects the zinc partial pressure during the reaction process for the growth of ZnO nanostructures [9]. Increasing the distance between source material and substrate decreases the vapour pressure and concentration of the reactant at the substrate position. This can affect the shape and size of the deposited structure. The growth process in our synthesis setup was enhanced by creating sharp temperature gradient between the source material and substrate (over short distance), which was assured by keeping the alumina tube on the substrate side open to air. Furthermore, the sprinkled zinc powder on the substrate has facilitated the growth by

contributing to the vapour concentration which leads to the bulk growth observed at the base of ZnO nanowires.

4.1.2. X-ray diffraction (XRD)

XRD is an important characterization technique that has long been used to address issues related to crystal structure of solids including lattice constants and geometry, identification of unknown material, orientation of single crystals, preferred orientation of polycrystals, defects, stresses etc [27]. In XRD, when a collimated beam of x-ray strikes the sample, it can be diffracted by the crystalline phase in the sample according to the Bragg law:

$$2d \sin\theta = n\lambda \quad \text{..... (4.1)}$$

where d is spacing between atomic planes in a crystalline phase, λ is wavelength of x-ray and n is the order of Bragg corresponding reflection. Thus, the intensity of the diffracted X-ray as a function of the diffraction angle (2θ) is measured. This diffraction pattern is used to identify the specimen's crystalline phases and to measure its structural properties. The interplanar spacing of the $(hk.l)$ plane in a wurtzite hexagonal structure can be related to the lattice constants c and a by [30]:

$$d_{hkl} = \frac{1}{\sqrt{\frac{4}{3a^2}\left(h^2 + k^2 + hk\right) + \frac{l^2}{c^2}}} \quad \text{..... (4.2)}$$

In this work, the phase and crystalline structure of as-synthesized ZnO nanowires was identified by Philips X'Pert MPD X-ray diffractometer which was operated at 40 kV and 50 mA to generate $Cu\,K_\alpha$ radiation of $\lambda = 1.5406$ Å and 1.54443 Å.

4.1.2.1 Results and discussion

Figure 4.4 shows a typical XRD pattern of the as-grown nanowires. Six diffraction peaks corresponding to ZnO at 2θ of 31.85º, 34.53º, 36.30º, 47.78º, 56.71º, and 63.18º indexed

as $(10\bar{1}0)$, (0002), $(10\bar{1}1)$, $(10\bar{1}2)$, $(11\bar{2}0)$ and $(10\bar{1}3)$, respectively were observed. These diffraction peaks are similar to the indexed peaks of wurtzite hexagonal phase bulk ZnO as reported in JCPDS card (No. 36-1451), indicating that the as-grown nanowires have wurtzite hexagonal structure. The XRD result can also suggest that the nanowires are randomly oriented which is in agreement with the observed SEM image.

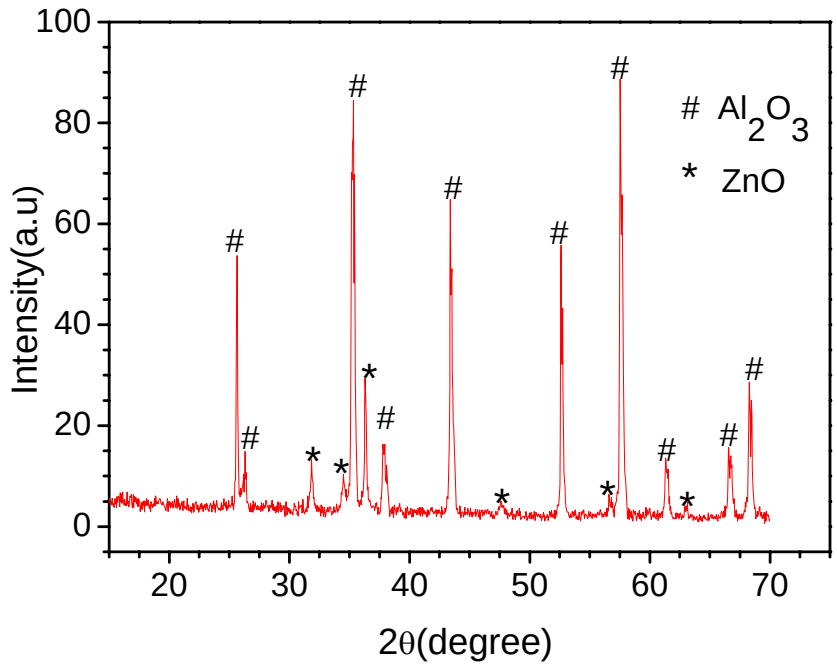

Figure 4.4-Typical XRD pattern of the as-grown ZnO nanowires.

In addition to the diffraction peaks of ZnO, intensive peaks corresponding to the substrate were also observed as indicated on the spectrum. The dominance of these peaks is due to the fact that XRD is taken from large area of the substrate surface, which is not uniformly covered with ZnO as can be seen from the SEM image. The absence of other diffraction peaks corresponding to unreacted Zinc or other crystal phases apart from the substrate is an indication to good crystallinity of the nanowires.

The lattice constants a and c of the as-grown ZnO sample can be calculated from the observed XRD pattern using the Bragg law and equation 4.2. From the peaks of ZnO $(11\bar{2}0)$ at 56.71º and ZnO (0002) at 34.53º with full width half maximum (FWHM) of

0.16 and 0.2, respectively, the lattice constants are deduced to be $a = 0.3250\ nm$ and $c = 0.5206\ nm$. A comparison with lattice constants of bulk ZnO ($a = 0.3249\ nm$ and $c = 0.5206\ nm$) [13] show that the as-grown sample is nearly free of homogenous strain. Moreover, the absence of broadening in the diffraction peaks confirms that the nanowires are free of inhomogeneous strain which usually originates from point defects and poor crystallinity [27]. The SEM image showed that the nucleation and growth of the nanowires did not occur directly on the substrate heterogeneously, rather on the bulk ZnO at the base. This avoids the lattice strain normally associated with lattice mismatch between ZnO and the alumina substrate. The in-plain lattice strain has been observed for ZnO nanorods grown on AlN [31].

4.2 Optical characterization

Optical spectroscopy has been widely used for characterization of nanomaterials. These techniques can be generally categorized into two main groups: absorption and emission spectroscopy and vibrational spectroscopy [27]. The former determines the electronic structure through excitation and relaxation of electrons while the latter provides structural information through vibrational excitation and phonon scattering. In this study, optical properties of the as-grown nanowires were investigated using steady state Photoluminescence and Raman scattering including micro-photoluminescence and micro-Raman characterization.

4.2.1 Raman spectroscopy

Raman spectroscopy has been established among the optical methods as fast, sensitive and non-destructive method for investigation of the crystallinity and homogeneity of materials as well as its electronic properties [32]. It can provide structural information such as, crystalline quality, layer orientation, and stress of semiconductor nanostructures. The presence of phonon peak in the Raman spectra depends on the selection rules which can be established from symmetry considerations. Therefore, with the application of this symmetry selection rules, one can identify the lattice structure as well as orientation using different scattering geometries and polarization. The selection rule for Raman scattering of wurtzite crystals including ZnO is shown in table 4.1.

Table 4.1-Raman selection rule for wurtzite-type crystals [32].

Phonon wave vector (q)	**Geometry**	**Parallel (HH) Polarization**	**Crossed (VH) polarization**
$q // \hat{c}$	Backscattering	$A_1(LO), E_2$	E_2
$q \perp \hat{c}$	Backscattering	$A_1(TO), E_2$	$E_1(TO)$
	90º scattering	E_2	$E_1(TO), E_1(LO)$

4.2.1.1 Experimental description

Vibrational properties of the as-grown nanowires were investigated using both nonresonant and UV resonant Raman scattering. The nonresonant Raman spectroscopy measurements were carried out with a Jobin Yvon T6400 micro-Raman system consisting of double monochromator in a subtractive configuration. An Ar^+ laser (514.5 nm) was used as excitation source. The light from the sample was collected using Olympus optical microscope with 100x objective which gives a resolution of 1 cm^{-1}. The spectra were then recorded using liquid nitrogen-cooled spectrum One CCD detector. In the resonant Raman scattering, He-Cd laser (325 nm) was used to excite the sample and the spectrum was analysed in backscattering geometry using Horiba (Jobin-Yvon HR 800) micro-Raman spectrometer with 2400 grooves/mm gratings. All spectral measurements were taken at room temperature.

4.2.1.2 Results and discussion

Figure 4.5 shows the typical Raman spectrum of ZnO nanowires measured with the 514.5 nm laser line excitation source. The remarkable peak at 436.8 cm^{-1} is assigned to the $E_2(high)$ mode of ZnO while the relatively weak peak at ~580 cm^{-1} results from the polar symmetry $E_1(LO)$ phonon mode. The two short peaks observed at 330.2 cm^{-1} and 379.6 cm^{-1} are attributed to the $E_{2H} - E_{2L}$ (multi-phonon) and $A_1(TO)$ modes, respectively [12]. The presence of the high intensity and sharp $E_2(high)$ mode confirms that the synthesized nanowires have wurtzite hexagonal structure with good crystalline quality.

In backscattering geometry, the $E_1(LO)$ mode is theoretically forbidden according to the Raman selection rule. Nevertheless, it can be still visible if the incident direction of the excitation laser light with respect to the crystal axis is not well defined in the use of the focusing lens for micro-Raman measurement. The misalignment of the nanowires has been also proposed for the appearance of this phonon mode in the backscattering geometry [10,12]. The SEM observation and XRD pattern showed that the nanowires are not well aligned, and hence the possibility of observing the $E_1(LO)$ mode.

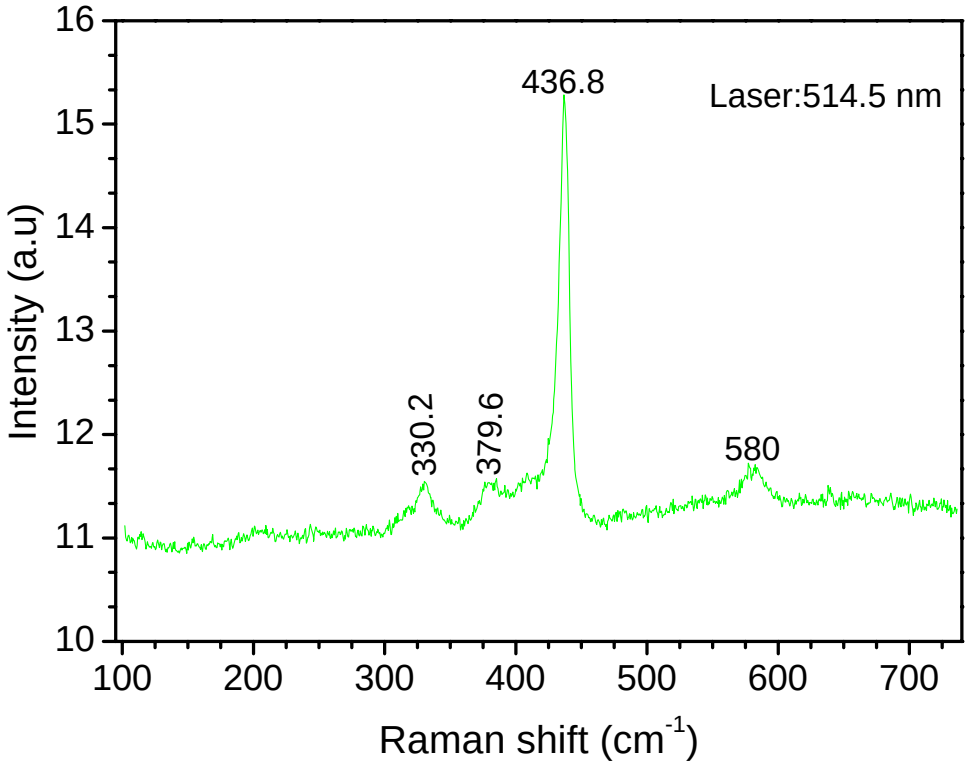

Figure 4.5-Typical off-resonant Raman spectra of as-grown nanowires taken under accumulation time of 100s.

The peak at 436.8 cm^{-1} which corresponds to $E_2(high)$ mode is shifted to lower frequency by ~3 cm^{-1} as compared to the bulk ZnO. Three possible mechanisms have been proposed for the phonon peak shift and line width broadening in Raman spectra of nanostructures including nanowires [33]: the phonon confinement effect due to nanosized of the material, phonon localization by defects or impurities, and lattice strains. Considering the high

sensitivity of $E_2(high)$ mode to a stress, the observed slight redshift of this peak could be due to lattice strain.

The vibrational properties of the nanowires were also further investigated using UV resonant Raman scattering. Typical spectrum taken with 40s accumulation time from ~1.5 mm spot diameter is shown in figure 4.6. Two major bands, centred at 570 cm^{-1} and 1145 cm^{-1} with band widths of 19.2 cm^{-1} and 32.8 cm^{-1}, respectively were observed. These bands are attributed to the first and second order scattering of LO phonon modes in ZnO.

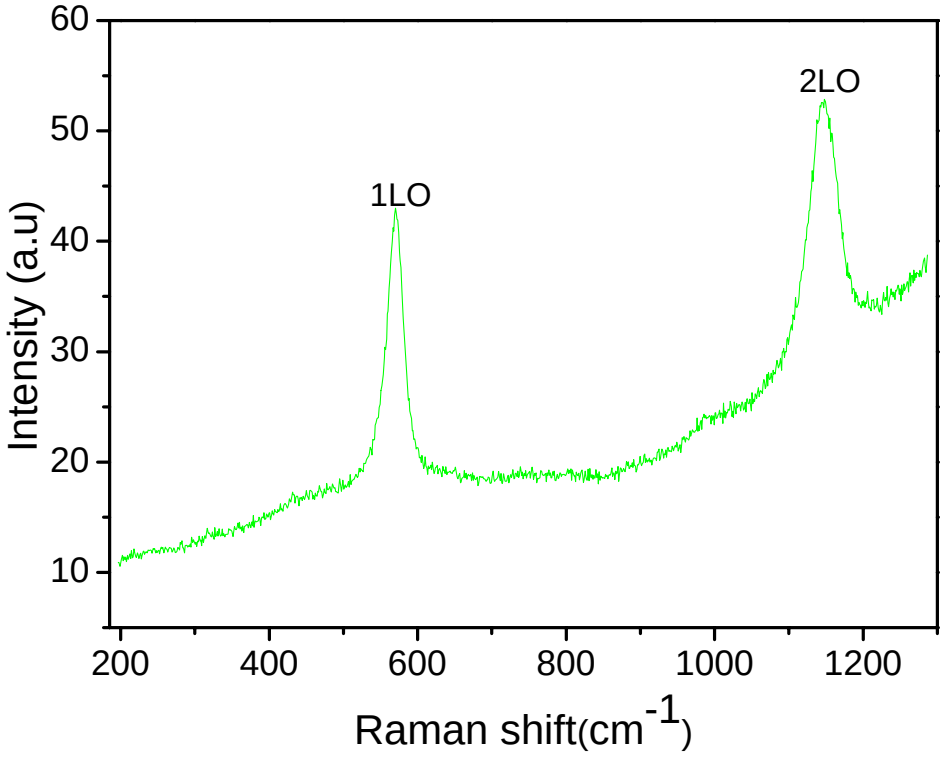

Figure 4.6-Resonant Raman spectrum of ZnO nanowires obtained using He-Cd (325 nm) laser line excitation at room temperature.

In resonant Raman scattering, the exciting photon energy is in resonant with the electronic interband transition energy of the wurtzite hexagonal phase ZnO, and the polar symmetry makes the LO phonons to be the dominant modes. According to the Raman selection rule for wurtzite crystals the LO line could be A_1 or E_1 mode, whose frequencies are different by $\approx 10\ cm^{-1}$, depending on the scattering geometry. However, these two modes can not be

distinguished due to the random alignment of the nanowires which makes the sample isotropic. Therefore, the first-order (1LO) Raman mode observed at 570 cm^{-1} can be attributed to the superposition of the polar symmetry modes $A_1(LO)$ and $E_1(LO)$, and their overtones.

In bulk ZnO, the $A_1(LO)$ phonon mode peaks at ~574 cm^{-1} while $E_1(LO)$ is observed at ~585 cm^{-1} [17,34]. Accordingly, the 1LO-phonon frequency should be between ~574 cm^{-1} and ~585 cm^{-1}. But, the observed 1LO-phonon is shifted to lower frequency with peak at 570 cm^{-1}. This shift can be explained as follows. Phonon eigenstates in an ideal crystal are plane waves due to the infinite correlation length and therefore, the $q \sim 0$ momentum selection rule of the first-order Raman spectrum can be satisfied. In the contrary, for nanostructures with dimensions in the nanometre scale, momentum selection rule is relaxed allowing the participation of phonons away from the center of the first Brillouin-zone. This gives rise to redshift and asymmetric broadening of the Raman peaks in nanostructures compared to the bulk crystals [17]. As a consequence, phonon modes of nanostructures including nanowires show discrete spectrum of frequencies different from those of bulk phonons. The observed redshift in the LO phonon peak of the nanowires can also be attributed to the intense local heating induced by the UV laser. This phenomenon has been proved for ZnO nanocrystals with average diameter of 20 nm [17].

The line widths of 1LO and 2LO scatterings for our ZnO nanowires can not be explained by the equation, $\sigma(nLO) = 9n(cm^{-1})$ which has been theoretically predicted for bulk ZnO [35]. The origin of this broadening has been ascribed to various sources such as, spatial confinement of phonons, lattice strain, and localization of phonons by defects [17,33]. The XRD result showed that the nanowires are nearly strain-free. This is an indication for the observed phonon line width broadening to be unlikely due to the lattice strain. Therefore, the broadening of the LO phonon bands is more likely due to the confinement of phonons in the nanowires which allows the participation of phonons away from the centre of Brillouin zone. A similar line width broadening effect has been observed in ZnO nanowires epitaxially grown on GaN buffer layer and m-sapphire substrate [36,37], and attributed to phonon confinement.

4.2.2. Photoluminescence

Luminescence refers to all types of emission appearing as consequence of some external excitation, except incandescent emission [18]. Depending on the source of excitation, luminescence is classified as photoluminescence (PL) with light excitation, cathodoluminescence (CL) with electron beam excitation, electroluminescence with electric field excitation source, chemoluminescence as result of chemical reaction, and so on. The photon emission of a semiconductor is the direct result of electron transition from higher energy level to lower energy levels. Thus, information about the electronic structure of semiconductor could be obtained from the analysis of the luminescence spectra.

4.2.2.1 Basic principles of PL

When electrons are excited across the bandgap of a semiconductor by means of excitation with photon energy $h\nu \geq E_g$, they move into the allowed excited state in the conduction band. These excited electrons may move freely, or correlated with the holes via coulomb interaction as pseudo-particles called excitons, until they recombine. When these electrons return to their equilibrium state, the excess energy is released either as light (a radiative process) or by non-radiative process, as conversion into lattice phonons. In spectroscopy, the spectral distribution of the emitted photons is referred as *emission spectrum*.

The emission spectrum is related to the energy difference between the two electron levels involved in the transition, i.e., between the excited and ground states. The intensity of the emitted light is related to the quantum efficiency, excitation power density and absorption of the exciting light. Increasing the excitation power density increases the number of photons, and therefore the number of photoexcited electrons. As radiative emission is not the only mechanism by which the electrons in the excited state can drop down to the ground state, the quantum efficiency is the relative contribution of the radiative process to the total energy released (radiative and non-radiative). The electronic states of the atoms or molecules in a solid are strongly coupled to the vibrational modes of the crystal through the vibronic interaction. This has effect on the absorption and emission spectrum. Therefore, it is important to have some general idea of recombination dynamics as well as electronic-vibrational interaction before dealing with the recombination channels leading to radiative transitions in ZnO.

4.2.2.2 Recombination dynamics

Electrons in an excited state can relax to the ground state through either radiative or non-radiative transitions. In non-radiative transition, the electron may lose its excitation energy as heat by emitting phonons or, may transfer the energy to impurities/defects.

The spontaneous emission rate for radiative transition between two electronic energy level depends on the population (N) of the excited state at time, t. This relation is given as [38]:

$$(\frac{dN}{dt})_{rad} = -AN \quad \text{..... (4.3)}$$

This leads to;

$$N(t) = N(0)\exp\left(\frac{-t}{\tau_R}\right) \quad \text{..... (4.4)}$$

where $\tau_R = \frac{1}{A}$ is the life time of the radiative transition and A is the *Einstein coefficient*.

The luminescence efficiency, which depends on the relative contribution of radiative and non-radiative process, can be calculated by writing down the rate equation for the population of the excited state when non-radiative transition is possible.

$$\left(\frac{dN}{dt}\right)_{total} = \frac{-N}{\tau_R} - \frac{N}{\tau_{NR}} \quad \text{..... (4.5)}$$

Therefore, the luminescence efficiency η_R is given by the ratio of equation (4.3) and (4.5) as:

$$\eta_R = \frac{1}{1+\tau_R/\tau_{NR}} \quad \text{..... (4.6)}$$

On the other hand, non-radiative transitions are thermally activated and the equilibrium transition rate using the classical *Mott* model is given by:

$$W_{NR} = W_0 \exp\left(\frac{-E_a}{k_B T}\right) \quad \text{..... (4.7)}$$

where W_0 is the non-radiative transition rate at T= 0K, and E_a is the activation energy of non-radiative recombination.

Therefore, the luminescence efficiency can be defined as:

$$\eta = \frac{W_R}{W_R + W_0 \exp\left(\frac{-E_a}{k_B T}\right)} \quad \text{..... (4.8)}$$

Moreover, the efficiency and the PL intensity can be related by the expression [23]:

$$\frac{\eta(T)}{\eta(T=0)} = \frac{I(T)}{I(T=0)} \quad \text{..... (4.9)}$$

Setting the quantum efficiency at low temperature to unity, the temperature dependency of emission intensity can be expressed as:

$$I(T) = \frac{I_0}{1 + a \exp\left(\frac{-E_a}{k_B T}\right)} \quad \text{..... (4.10)}$$

where $a = \frac{W_0}{W_R}$ is the ratio of non-radiative (T = 0K) and radiative transition probability .

In general, the temperature dependency of PL intensity involving i non-radiative recombination channels is given by:

$$I(T) = \frac{1}{1 + \sum_{j=1}^{i} a_j \exp\left(\frac{-E_{a_j}}{k_B T}\right)} \quad \text{..... (4.11)}$$

In this way, the temperature dependence of the intensity of various transition lines can be used to identify the activation energies of the center involved in the quenching mechanism.

4.2.2.3 Radiative transition and vibrational coupling

The optical transition involving the coupling of vibrational (phonon) modes and electronic levels can be understood by invoking the *Frank-Condon* principle. This states that electronic transitions take place so rapidly that the nuclei do not move significantly during

transition. The principle follows from the *Born-Oppenheimer* approximation, which states that the electronic and nuclear motions are independent, and one can draw the electronic energy as a function of internuclear separation. The approximation bases on the fact that the nuclei are much heavier than the electrons, and move on a far slower time scale. The vibrational motion is described in terms of the normal modes of the coupled system. These vibrational modes are represented by a generalized coordinate Q, which has the dimension of length. The *Born-Oppenheimer* approximation thus allows us to produce configuration coordinate diagram (CCD) in which we plot the electronic energy as a function of Q. Figure 4.7 shows a typical CCD diagram for two electronic states ψ_a and ψ_b of a vibronic system. The optical transitions are indicated by vertical line as prescribed by *Frank-Condon* principle. Since the electron-lattice coupling of the two electronic states may differ, their equilibrium positions generally occur at different values of configuration coordinate.

Assuming the same vibrational frequency for the two electronic states ψ_a and ψ_b, the ionic potential energy of the states can be given as [39]:

$$E_a(Q) = \frac{1}{2} M\omega^2 (Q - Q_0)^2 \quad and$$
$$E_b(Q) = E_{ab} + \frac{1}{2} M\omega^2 (Q - Q_0)^2 - A\hbar\omega(\frac{M\omega}{\hbar})^{\frac{1}{2}}(Q - Q_0) \qquad \text{..... (4.12)}$$

where the dimensionless constant $A = (\frac{M\omega}{\hbar})^{\frac{1}{2}}(Q_0^{'} - Q_0)$ characterizes the difference in electron-lattice coupling between electronic states a and b, M is the effective mass of the mode and E_{ab} is the energy separation between the excited state (a) and ground state (b) potentials at $Q = Q_0$.

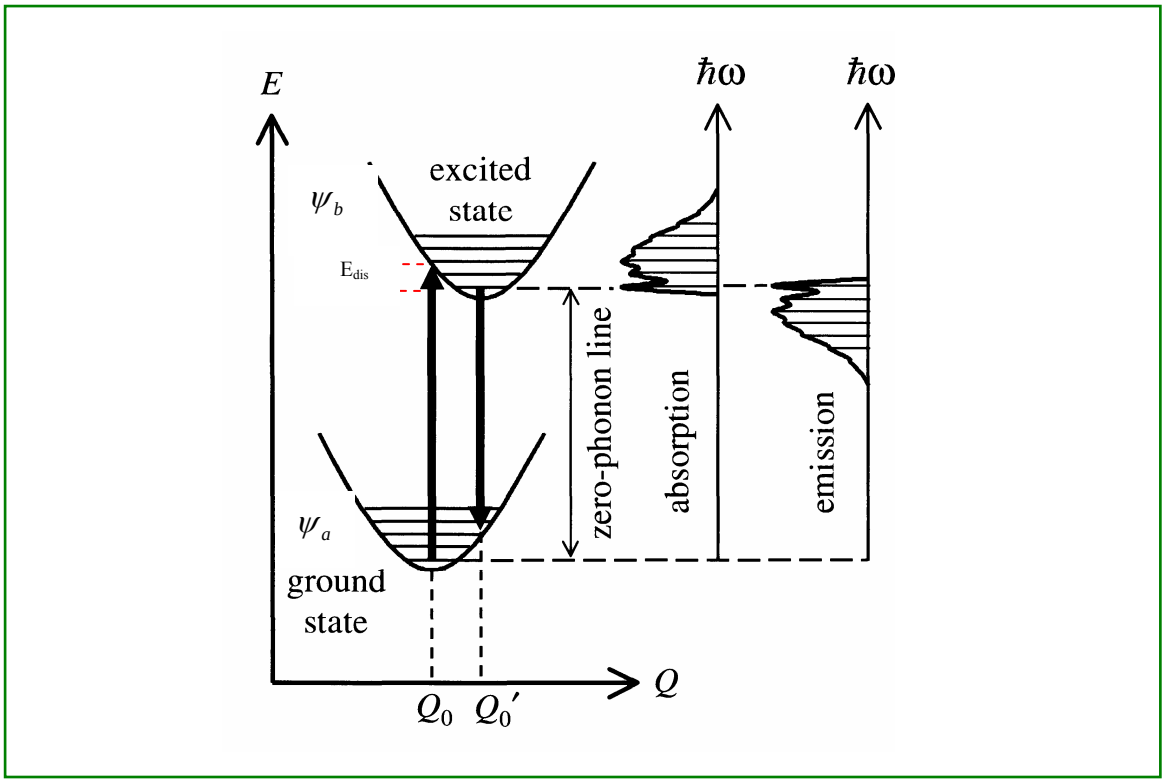

Figure 4.7-CCD diagram for the ground and excited electronic states of a vibronic solid. The optical transitions are indicated by the vertical arrows. The right hand side of the figure shows the general shape of absorption and emission spectra that would be expected [38].

For electronic-vibrational state a,m in the ground state and electronic-vibrational state b,n in the excited state, the complete set of wave functions can be written in linear combination as $\psi_a(r,Q)\chi_a(m)$ *and* $\psi_b(r,Q)\chi_b(n)$, respectively where r is the electron coordinate. Moreover, the quantum mechanical solutions for the vibrational states $\chi_a(m)$ and $\chi_b(n)$ are harmonic oscillator wave functions with eigenvalues given by:

$$\varepsilon_a(m) = (m+\frac{1}{2})\hbar\omega \text{ and } \varepsilon_b(n) = (n+\frac{1}{2})\hbar\omega \quad \ldots\ldots\ldots\ldots\ldots\ldots\ldots\ldots (4.13)$$

The parameter A, which characterizes the difference in electron- lattice coupling, can be also replaced by another dimensionless constant, *Haung-Rhys* parameter (S) as [39]:

$$S = \frac{A^2}{2} = \frac{1}{2}\frac{M\omega^2}{\hbar\omega}(Q_0^{'} - Q_0)^2 = \frac{E_{dis}}{\hbar\omega} \quad \text{.....} \quad (4.14)$$

where E_{dis} is the measure of the difference in electronic-vibrational coupling strength at the electronic states ψ_a and ψ_b as defined in figure 4.7.

Therefore, the absorption and emission transitions between electronic states *a* and *b* can be analysed using this configurational coordinate. Accordingly, the absorption spectra can be given by:

$$E_n = (E_{ab} - S\hbar\omega) + n\hbar\omega = E_0 + n\hbar\omega \quad \text{.....} \quad (4.15)$$

where E_0 is the zero phonon line (ZPL) which corresponds to transition between zero vibrational levels of both initial and final states. The spectrum is peaked at n ~ S, which corresponds to E_{ab} as shown in figure 4.7. The corresponding emission spectrum also shows transition at:

$$E_m = E_0 - m\hbar\omega \quad \text{.....} \quad (4.16)$$

From equation (4.15) and (4.16), one can deduce that absorption transition begins in the lowest vibrational level of the ground state, while the emission line starts at the lowest vibrational level of the excited state. This gives rise to vibronic absorption and emission bands as shown in the right side of figure 4.7.

The intensity as well as band shape of the absorption and emission spectrum depends on the value of S .This dependence can be derived by considering the transition probability between the two electronic sates. The optical transition probability is proportional to the square of the matrix element of the wave functions as:

$$W \sim \left| < \psi_b(r,Q)\chi_b(n) | \mu | \psi_a(r,Q)\chi_a(m) > \right|^2 \quad \text{.....} \quad (4.17)$$

where the integration is over the electronic and vibrational coordinate and μ is the appropriate dipole operator (electric, magnetic).

In the C*ondon approximation* the electronic dipole moment is independent of the nuclear coordinate. Thus, the matrix element can be factorized as:

$$< \psi_b(r,Q)|\mu|\psi_a(r,Q) > < \chi_b(n)|\chi_a(m) > \text{ and}$$
$$W \sim P_{ab}|< \chi_b(n)|\chi_a(m) >|^2 \quad \ldots\ldots\ldots\ldots\ldots\ldots\ldots\ldots\ldots\ldots \quad (4.18)$$

where P_{ab} is the purely electronic transition probability and is the same for all vibrational transition states m,n. Therefore, the relative values of the transition probabilities depend on the squares of the vibrational overlap integrals. Although the two vibrational states are similar set of harmonic oscillator function, their values are defined with respect to different zeros of the coordinate Q. Therefore, the overlap integrals are in general not zero.
The overlap between displaced harmonic oscillator wave function is given by [39]:

$$< \chi_b(n)|\chi_a(m) >= \exp\left(\frac{-A^2}{4}\right)\left(\frac{m!}{n!}\right)^{\frac{1}{2}}\left(\frac{A^2}{2}\right)^{\frac{1}{2}(n-m)} L_m^{n-m}(\frac{A^2}{2}) \ldots\ldots\ldots\ldots\ldots\ldots\ldots\ldots \quad (4.19)$$

where L_m^{n-m} are associated Laguerre polynomials of which $L_0^m(x) = 1$.
Substituting for A, the normalized transition probability is then given by:

$$W_{nm} = \exp(-S)\left(\frac{m!}{n!}\right)S^{n-m}\left(L_m^{n-m}(S)\right)^2 \ldots\ldots\ldots\ldots\ldots\ldots\ldots\ldots\ldots\ldots\ldots\ldots\ldots\ldots\ldots\ldots \quad (4.20)$$

At absolute zero temperature, only the $m = 0$ vibrational state is occupied leading to $L_0^n(S) = 1$. The transition probability to the nth level of excited state thus becomes;

$$W_{n0} = \frac{S^n}{n!}\exp(-S) \ldots\ldots\ldots\ldots\ldots\ldots\ldots\ldots\ldots\ldots\ldots\ldots\ldots\ldots\ldots\ldots\ldots\ldots\ldots\ldots\ldots\ldots \quad (4.21)$$

The various transitions between the electronic states could involve different values of *Huang-Rhys* parameter, S, and this value determines the band shape and width in the emission and absorption spectra. Moreover, the relative intensity of the mth phonon replica (I_m) is related to the zero-phonon peak (I_0) by the S factor as $I_m = I_0\frac{S^m}{m!}\exp(-S)$. This can be used estimate the S factor, which determines the coupling strength of exciton to phonon, from the PL spectra.

4.2.2.4 Photoluminescence of ZnO

ZnO has been known to be a luminescent material for century. Optical properties of a various forms of ZnO, including ZnO nanostructures have been studied by photoluminescence. Room temperature PL spectra of ZnO typically consist of UV emission band and possibly one or more visible emission bands due to defects and/or impurities. The near UV-band is closely related to the excitonic nature of the material and may be superposed with the free exciton and its phonon replica, bound exciton emission as well as biexciton emission [5,13]. This band is split into several emission lines at low temperature, mainly at temperature as low as a few degree of absolute temperature. Low temperature PL measurements of bulk ZnO as well as different nanostructures such as, nanoparticles, nanowires, faceted nanorods, nanosheets have been reported in literature [5,17].

According to earlier reports in literature, the PL spectra of bulk ZnO in the near band-edge region has been categorized into seven regions as: free excitons (FE), excitons bound to ionized donors (D^+X), excitons bound to neutral donors (D^0X), excitons bound to neutral acceptors (A^0X), exciton complexes (EC) with deep centres, two-electron transition, and phonon replica region [29,40]. The typical energy positions corresponding to these transitions are labelled on a typical spectrum of ZnO film shown in figure 4.8.

The recombining electrons and holes in a semiconductor usually interact through a coulomb force which leads to the formation of excitons. Owing to this, the band to band transition is hardly detected in PL, and the spectra are dominated by excitonic emissions.

The luminescence energy corresponding to free exciton emission is given by:

$$E_{FX} = E_g(T) - E_{ex}^b \quad \text{..... (4.22)}$$

where, E_{ex}^b is the binding energy of free exciton.

The temperature dependency of the exciton peak position shows approximately the same behaviour as the bandgap. As stated earlier, the valence band in hexagonal wurtzite structures near $\vec{k} = \vec{0}$ splits into three separate bands labelled as A, B, and C, whose relative positions are determined by the combination of spin-orbit coupling and axial crystal field strength. It has been identified that the hole effective mass in ZnO is nearly isotropic and similar for the A, B and C valance bands, and hence the effective electron-

hole pair mass is determined by the electron mass [16]. Therefore, assuming that the binding energy of the *A, B*, and *C* excitons are nearly equal the difference in the observed exciton peaks due to transitions from the A, *B*, and *C* bands can be used to determine the splitting of the valence band. The energy separation between the three valence band energy levels of ZnO has been reported as $E_{AB} \approx 4.9\ meV$ and $E_{BC} \approx 44\ meV$ [20] though there is slight variation in different reports.

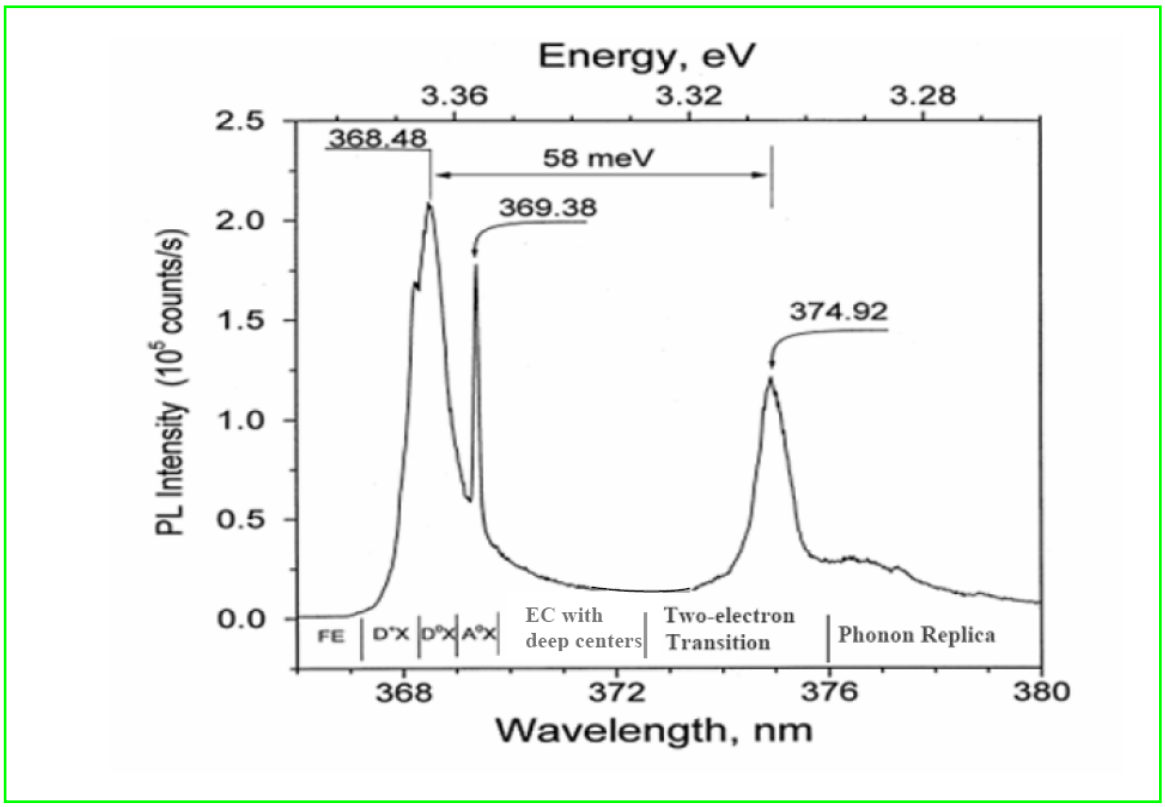

Figure 4.8-Low temperature PL spectrum of as-grown ZnO film in the band-edge region [40 with slight modification].

In a similar way as free carriers can be bound to point defects, excitons also tend to localize near neutral or ionized impurity/defect, and hence form exciton complexes. The energy with which the exciton is bound to donor or acceptor level is denoted by E_{loc}. Thus, the emission corresponding to the bound exciton becomes:

$$E_{Bx} = E_g(T) - E_{ex}^b - E_{loc} \quad \text{..... (4.23)}$$

It has been observed that the localization energy of exciton is highest for A^0X , lower for D^0X and still lower for D^+X [19]. On the other hand, ionized acceptors do not usually bind an exciton since a neutral acceptor and free electron are energetically more favourable.

The binding energy of the exciton to the complex depends on the chemical nature of the complex and on the surroundings, leading in high resolution spectroscopy to the splitting of the bound exciton lines. The complex (defect) center to which the excitons are bound can be foreign impurities or native defects. Low temperature PL spectra of high quality ZnO is usually dominated by several bound exciton emission lines (labelled as I_0-I_{11}) which correspond to neutral/ionized bound excitons. In nanostructures, these lines usually inhomogenously broaden and can not be clearly resolved [5]. The fine structures in the near band-edge region of intentionally undoped ZnO has been analysed by several authors [5,13,41]. A typical low temperature PL spectrum of ZnO sample exhibiting a number of bound-exciton peaks is shown in figure 4.9. Detail explanation of the observed peaks can be found in reference [5,13].

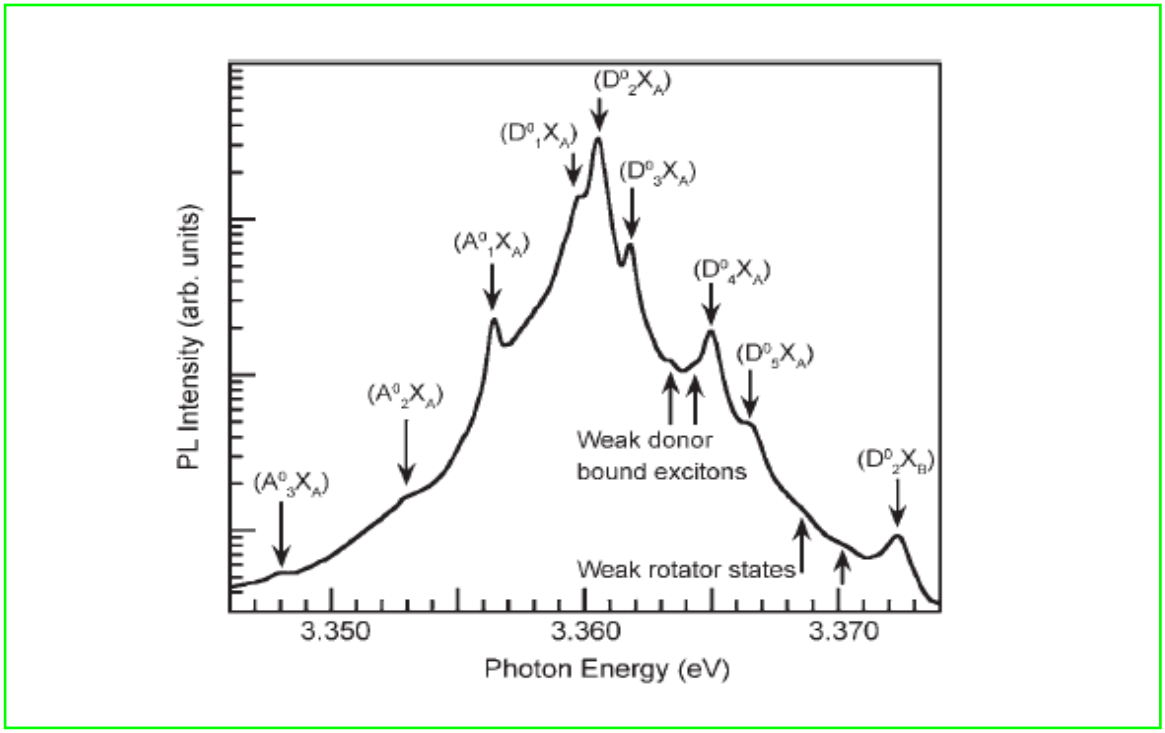

Figure 4.9-Bound exciton region of 10K PL spectrum for the forming gas annealed ZnO substrate [5].

The bound exciton complexes may have a certain excited states due to the various mutual arrangements and envelope functions of the two electrons (holes) and the hole (electron) in the $D^0X\,(A^0X)$ complex [19]. Moreover, recombination of exciton bound to a given center can be followed by ionization of the center. For instance, during recombination of an exciton bound to a neutral donor in ZnO, the donor final state can be 1s state (normal D^0X line) or the 2s, 2p state called as two-electron satellite (TES line) (see fig.4.8). In a simple hydrogen-like effective mass approach (EMA) the energy separation between n = 1 and n = 2 states would be ¾ of the donor binding energy (E_D). Accordingly, the splitting of the excited states can be correlated to the energetic distance of TES lines from their respective bound exciton lines and the donor binding energies as [20,42]:

$$E_{TES} = E_{D^0X} - (E_{D(1s)} - E_{D(2p)}) \quad \text{..... (4.24)}$$

With $E_{D(1s)} - E_{D(2p)} = \frac{3}{4}E_D$

Therefore, the determination of TES position with respect to the donor bound exciton peaks in the PL spectra can be used to estimate the donor binding energies. Moreover, the localization energy of exciton is linearly related to the binding energy (E_D) of the defect center according to *Haynes rule* as [42]:

$$E_{loc} = bE_D \quad \text{..... (4.25)}$$

More generally, this equation can be written as:

$$E_{loc} = a + bE_D \quad \text{..... (4.26)}$$

where a and b are constants to be determined from experiment and depends on the type of defect. This linear dependence of the exciton localization energy on the donor binding energy (E_D) has been clearly observed for ZnO [13, 42,43]. For instance, Meyer *et al*. [43] found the relation as $E_{loc} = 0.37E_D - 4.2\ meV$ for neutral donors and $E_{loc} = 0.5E_D - 23\ meV$ for ionized donors.

The near band-edge low temperature PL spectra of ZnO can also contain the donor–acceptor (DAP) transitions. When the wave function of an electron trapped at a donor

overlaps with the wave function of hole located at acceptor level they can recombine radiatively. After recombination a positive effective charge is left in the donor and a negative effective charge in the acceptor level. Thus, the final state is determined by the coulomb potential interaction between them (which is given by $\frac{-e^2}{4\pi\varepsilon R}$), where ε is the dielectric constant of the crystal and R is the distance between the donor and acceptor. Therefore, the photon resulting from the DAP recombination involving phonon emission is given by [19]:

$$E_{DAP} = E_g - E_A - E_D + \frac{e^2}{4\pi\varepsilon R} - m\hbar\omega_{LO} \quad \text{..... (4.27)}$$

where, E_D and E_A are the ionization energies of the neutral donor and acceptor, respectively, and the last term corresponds to the phonon replicas.

The DAP emission strongly depends on the excitation intensity as well as temperature. With increasing the excitation intensity, the number of occupied donor and acceptor increases and their average distance R decreases. As a consequence, one finds that the emission maxima of the pair band shifts to blue with increasing excitation due to the coulomb term in the equation (4.27). Moreover, the DAP emission intensity decreases with increasing temperature since the impurity with smaller binding energy (most probably donor impurity) is ionized at higher temperature.

Another transition line observed in the near band-edge PL of ZnO is the LO phonon replica. In the low temperature PL spectra, the DAP and the LO phonon replicas of ZnO usually lies in the same energy region, and hence requires great care in assigning the peaks [5]. The LO phonon energy can be determined from the separation between the exciton peaks and their phonon replicas, and for ZnO it is found to be 71-73 meV [5].

4.2.2.5 Description of PL measurement setup

Photoluminescence (PL) characteristics of ZnO nanowires were measured using Ik Series He-Cd laser (325 nm) of 200 mW as the excitation source. A schematic diagram of the PL measurement setup is shown in figure 4.10. A continuous wave excitation was provided by the laser. After passing through a narrow-band pass filter and an iris used to remove

both laser sidebands and stray light, the laser beam was focused on to the sample which is mounted in closed cycle helium cryostat. The generated light is collected in 45 ° geometry by an array of lens system and then focused onto the entrance slit of Spex 1704 monochromator equipped with 1200 mm^{-1} grating. The dispersed light is detected by cooled Hamamatsu R928 photomultiplier, and the emission spectrum as a function of wavelength is recorded.

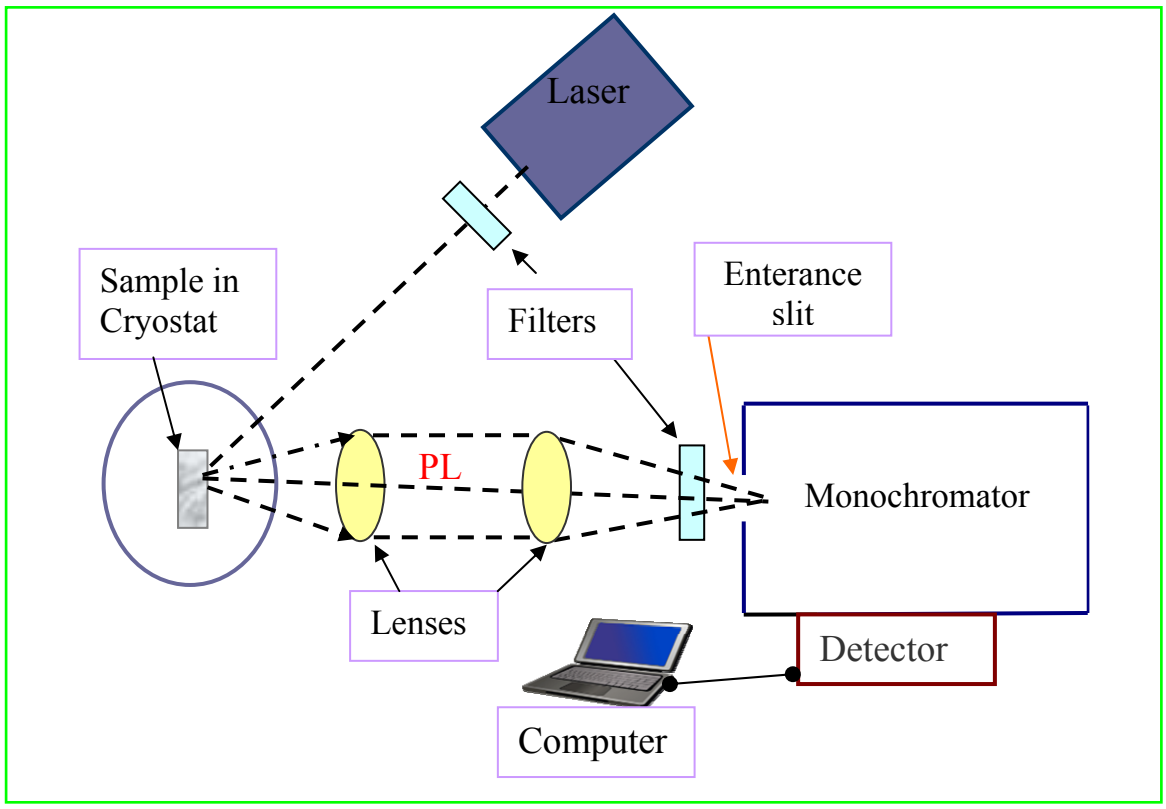

Figure 4.10-General view of the experimental setup for PL spectroscopy measurement.

4.2.2.6 Results and discussion

The PL spectra of the sample were studied both at low temperature (10K) and room temperature. In addition, the temperature dependence of near band-edge emission lines was studied in detail.

Figure 4.11 shows the PL spectrum of as-grown ZnO nanowires at 10K over a broad range of wavelengths. The feature of the spectrum can be categorized into two regions: the fine structure emission lines in the near band-edge region and unstructured green emission band centred at ~ 2.4 eV. The latter has been extensively studied for its undesirable effects on carrier lifetime and UV emission efficiency, and it has been associated with excess Zn,

oxygen vacancy, or surface state emission [44,45]. Among these factors, the singly ionized oxygen vacancy was found to play great role for green emission band [12,33,45]. Moreover, three models have been proposed to correlate the green emission with the singly ionized oxygen vacancy (V_O^{1+}). Accordingly, the green emission results from:

(i) radiative recombination of the photo-generated hole with the electron which belongs to the singly ionized oxygen vacancy,

(ii) recombination of a conduction band electron with doubly ionized oxygen vacancy (V_O^{2+}) centres, where the recombination center (V_O^{2+}) can be created when singly ionized oxygen vacancy traps a hole, and

(iii) donor to acceptor transition mechanism (DAP), where the donor and acceptor are assumed to be singly ionized oxygen vacancy (V_O^{1+}) and zinc vacancy (V_{Zn}^{2-}), respectively.

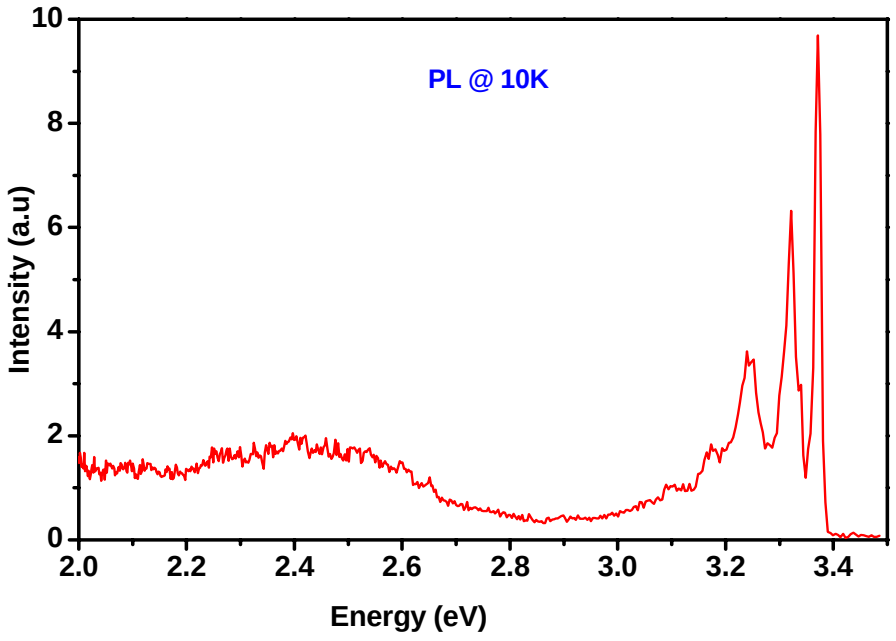

Figure 4.11-PL spectra of the as-grown nanowires at 10K over broad range of wavelength obtained with above bandgap excitation.

In addition to the intrinsic defects, there has been an argument that impurities like Cu are also responsible for the green emission band [5,46 and references therein].

Furthermore, it has been reported that the green band related to intrinsic defects are unstructured while structured green band emissions are observed for Cu impurities [47]. Accordingly, the unstructured nature of the observed green emission suggests that it is likely due to the intrinsic defects. Nevertheless, there is no consensus in literature about the chemical nature of the defect responsible for the green emission, and it has not yet been conclusively identified.

The ratio between the PL intensity of the excitonic recombination and the deep level emission is usually identified as a measure of the optical quality of the sample. Moreover, the higher structured near band-edge recombination (figure 4.11 and 4.12) indicates a good crystallinity of the nanowires. This is in agreement with the XRD and Raman scattering results.

Figure 4.12 shows high resolution near band-edge PL spectrum of the as-grown sample obtained at 10K. The inset shows the details of PL features related to various exciton (zero-phonon) emissions. As commonly observed in ZnO, the spectrum is dominated by radiative decays from bound exciton complexes with the strongest peak at 3.369 eV. According to the energy position and convention for PL spectra of bulk ZnO, this peak corresponds to a neutral donor bound exciton (D^0X) emission line [40]. In addition, the second high intensity peak observed at 3.374 eV also lies in the ionized donor bound exciton (D^+X) emission region. However, similar peaks have been assigned to different origin in various reports. For instance, in bulk ZnO, Teke *et al*. [13] assigned the recombination line at 3.3686 eV to rotational excited states of neutral donor bound exciton. Recently, Meyer *et al*. [43] based on magneto-optical experiments suggested that the two emission lines at 3.3689 eV and 3.374 eV correspond to ionized donor bound exciton. On the other hand, a peak at 3.37 eV was observed in PL spectra of ZnO nanowires grown on alumina by the VLS mechanism and assigned to neutral donor bound exciton [44]. Another peak at 3.376 eV has been also observed in low temperature (10K) PL spectra of single crystal ZnO nanorods grown on sapphire and attributed to free exciton emissions [48]. The controversy in the assignment of these peaks could be partially due to variations in sample quality which also depends on the synthesis condition. Therefore, careful analysis of these emission lines is required in order to obtain intrinsic properties of the nanowires. The various emission lines arising from radiative decay of excitons evolves in a different way

with temperature, and hence the temperature dependent PL measurement can be used to identify the different excitonic emission lines.

Detailed temperature dependent analysis of the PL spectrum of the nanowires in the near band-edge region revealed that the peak at 3.369 eV is ascribed to donor bound exciton (D^0X) while the peak at 3.374 eV is more likely attributed to the free exciton (FXA) line. The broadening of the FXA emission line as shown in the inset of figure 4.12 is due to overlapping with the relatively weak donor bound exciton emission lines in the region. The temperature evolution of these peaks will be discussed later. A small hump at 3.383 eV on the high energy side of FXA could be attributed to free exciton B (FXB) or excited state of FXA (n=2). However, the energy separation between this line and the FXA lies in the range of previously reported energy gap of FXA and FXB [13,22]. Therefore, the peak can be tentatively assigned to FXB.

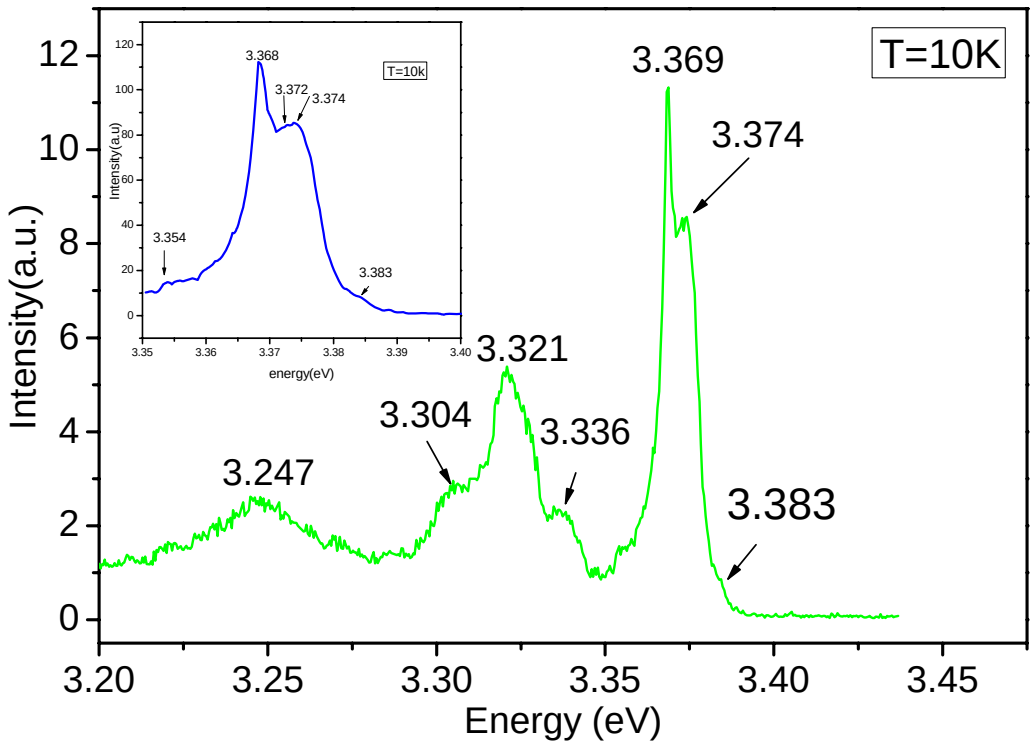

Figure 4.12-High resolution low temperature (10K) PL spectrum of the as-grown ZnO nanowires in the near band-edge region obtained using 325 nm laser excitation. The inset shows high resolution of the excitonic emission region.

In addition to the near band-edge exciton emissions (zero-phonon line), a series of PL spectral features could be observed between 3.336 and 3.304 eV as shown in figure (4.12). The peak at 3.321 eV next in intensity to the 3.374 eV line is commonly observed in PL spectra of ZnO. Different radiative recombination channels have been considered as the origin of this band including, phonon replica and two-electron satellite (TES) of donor bound exciton [5,20]. If we consider the energy gap between the observed exciton emission lines, the distance of 3.374 eV and 3.369 eV line from the 3.321 eV line is 53 meV and 48 meV, respectively. These energies are substantially smaller than the energy of longitudinal optical phonon in ZnO, which lies in the range of 70-73 meV [5,40]. This signifies that the line at 3.321 eV can not be assigned as LO phonon replica of the emission line at 3.374 eV or 3.369 eV. Therefore, based on the energy separation and the observed temperature dependence, it is more likely for this line to be the two-electron satellite (TES) of the neutral donor bound exciton at 3.369 eV. As stated earlier, the two-electron transition corresponds to the radiative recombination of donor bound excitons which leaves the donor in an excited state. Assuming that the excited states are hydrogenic, the energy separation between 3.369 eV and the TES line, 48 meV, can be used to estimate the donor binding energy as 64 meV. Furthermore, using Haynes rule and the relation obtained by Meyer *et al*. [43] for neutral donor bound exciton in ZnO ($E_{loc} = 0.37E_D - 4.2\ meV$) the exciton localization energy can be estimated as 19.48 meV. This value of exciton localization energy is in the same order with the energy difference between the FXB and D^0X line. However, the PL data is not sufficient to identify the chemical nature of the associated impurity. It could be due to extrinsic impurity contamination or intrinsic defects taking the shallow donor energy levels.

In figure 4.12, a shoulder seen at 3.304 eV on the low energy side of the TES peak is located at 70 meV from the excitonic emission line at 3.374 eV. Based on the energy separation, this peak can be attributed to the LO phonon replica of FXA line which results from the simultaneous emission of photons and phonons in the annihilation process of free excitons. On the other hand, phonon replica of the FXB is not clearly observed due to overlapping with the TES line. Another broad peak at 3.247 eV can be assigned to the donor-acceptor pair (DAP) transition commonly observed in bulk ZnO. In a DAP transition, the transition energy depends on the donor-acceptor distance (equation 4.27), and it is very unlikely that the distance is the same for all pairs. Thus, we expect a broad

PL peak corresponding to this transition, which is clearly observed for the peak at 3.247 eV. Finally, the peak at 3.336 eV is assigned to an exciton bounded to complex defects (e.g. Deep centres, and/or structural defects). It is close to the energy of 3.333 eV reported by Meyer *et al*. [20] for exciton bound to structural defects.

4.2.2.6.1 Temperature dependence of PL

In order to provide additional support for the peak assignments in the low temperature PL spectrum, the temperature evolution of the observed peaks were studied over a temperature range of 10K to room temperature. Figure 4.13 shows the temperature dependent near band-edge PL spectra in the range of 10-190K. The low temperature spectrum is dominated by the peak at 3.369 eV. This luminescence line becomes weaker with increasing temperature and eventually suppressed by the peak at 3.374 eV for temperature above 50K. For further illustration, the temperature variation of luminescence intensity for the excitonic emission lines in the low temperature region (10-100K) is shown in figure 4.14. The observed relative change in intensity of the D^0X and FXA lines can be explained by the fact that D^0X line is replaced by the free exciton (FXA) line, due to the ionization of neutral donor bound excitons with increasing temperature. More precisely, the fast quenching of the peak at 3.369 eV relative to 3.374 eV signifies that the peak at 3.374 eV is not attributed to bound exciton line, and hence supports the assignment of peaks at 3.369 eV and 3.374 eV to D^0X and FXA, respectively.

It is noted that the quenching of D^0X line is also followed by significant appearance of the peak at 3.383 eV, which was tentatively assigned to FXB. As the temperature increase, the FXB band becomes stronger in intensity relative to the FXA emission, and overtakes the FXA line for temperature above 70K. Moreover, the emission of this exciton line showed a shift to lower energy with increasing temperature and can bee seen up to room temperature, which supports the assignment of the peak at 3.383 eV to free exciton (FXB). Nevertheless, for temperatures above 190K, the convergence of free exciton, and coupling of the 1LO- phonon replica with the line broadening of each peaks has suppressed accurate determination of the free exciton peak position. Consequently, the room temperature peak should be considered as combination of these multiple peaks. Room temperature PL spectra will be discussed later.

In the lower temperature region (below 30K), the intensity of TES of D^0X follows the same trend as the D^0X line. Meanwhile, the peaks at 3.304 eV, 3.321 eV, and 3.336 eV as well as the LO phonon replicas of the FXB combine and results in broader emission band. In respective of the disappearance of FXA and D^0X line, the peak in the TES emission region is clearly observed up to 150K. This could be due to the contribution from the LO phonon replica of the FXB, which can survive to relatively higher temperature. The line width of the peak at 3.247 eV, which was assigned to the DAP emission, increases with temperature and can be observed until 80K. This broadening is due to overlapping of the DAP emission with the 2LO-phonon replica of the FXB.

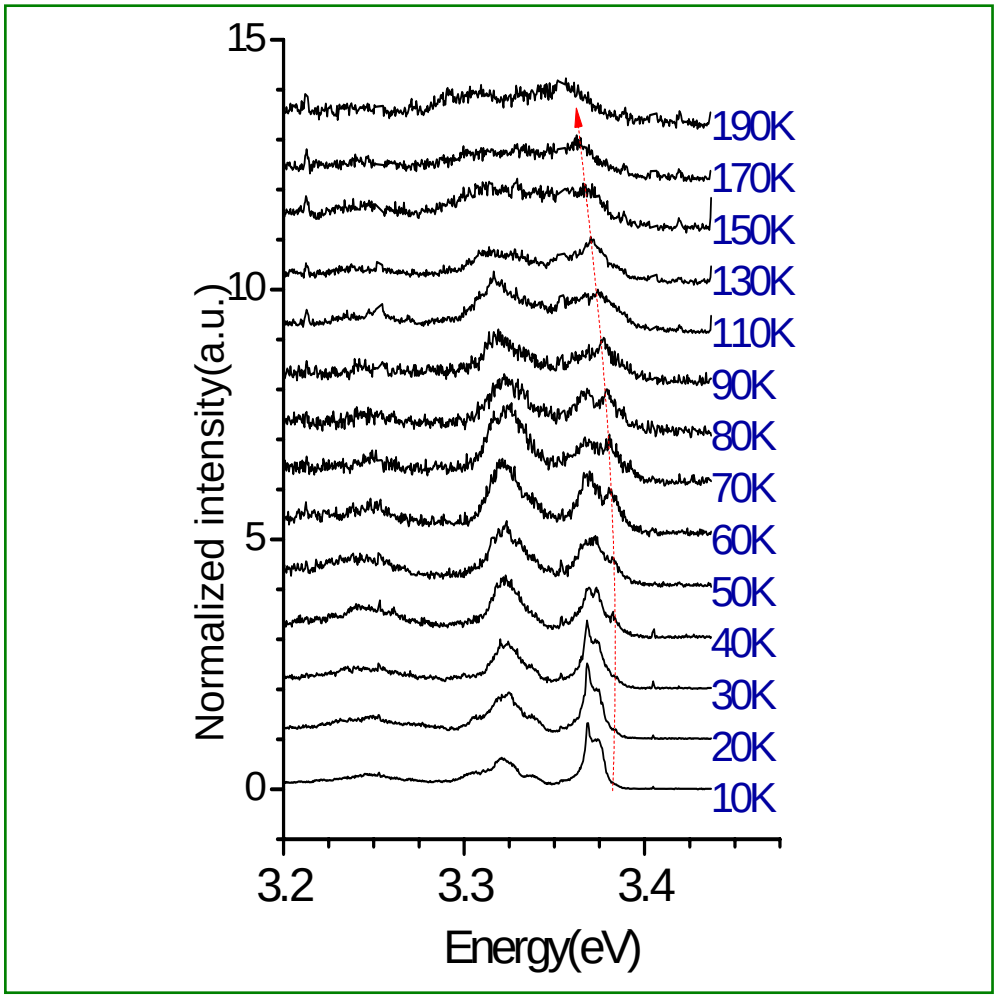

Figure 4.13-Temperature dependent PL spectra of ZnO nanowires measured with 325 nm laser excitation**.**

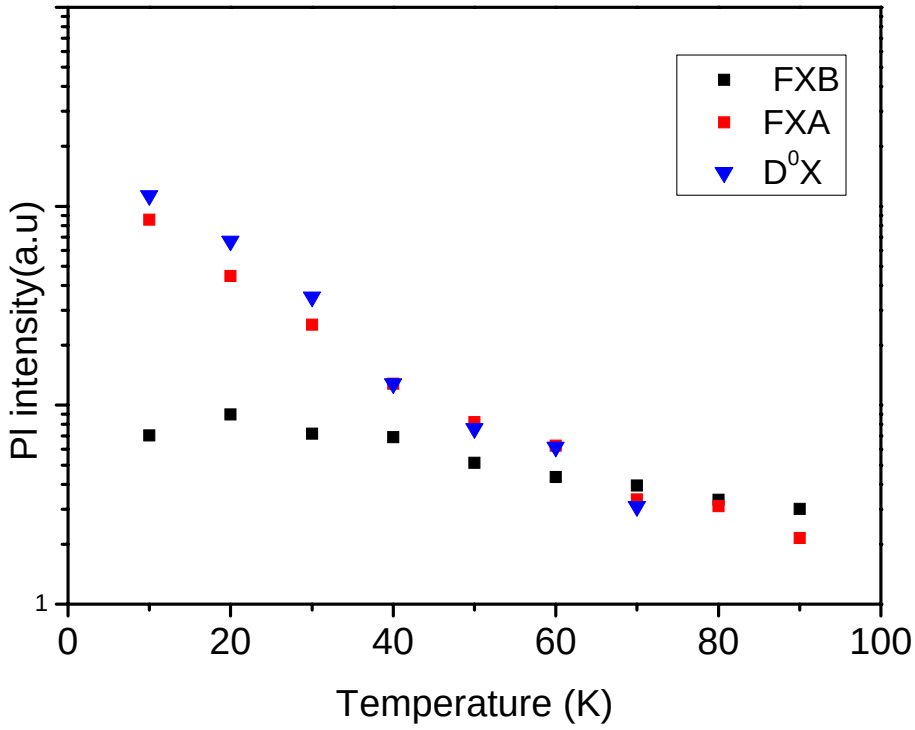

Figure 4.14-Temperature dependent PL peak intensities of the nanowires. The higher temperature region is omitted for clarity.

Figure 4.15 shows the temperature variation of the excitonic peak positions assigned to FX and D^0X emission in the temperature range of 10-190K. The free exciton emission lines show a non linear relationship and tend to shift to lower energy with increasing temperature. However, the neutral donor bound exciton line is negligibly shifted with temperature (for the observed temperature range). The temperature dependence of the excitonic emission lines is related to the relative position variation between the conduction and valence bands due to the temperature-dependent dilatation of the lattice and the temperature-dependent electron-lattice interaction [22]. Therefore, by assuming that the energetic distance between the bandgap edge and exciton energy level is independent of temperature, the obtained data can be fitted using the well known Varshni formula (equation 2.1). For comparison, the temperature variations of the bandgap corresponding to $A(\Gamma_7)$ and $B(\Gamma_9)$ degenerate valence bands are included in figure (4.15) as shown by open

and closed circles. These values are obtained by adding the corresponding exciton binding energy of 60.8 meV and 59.1 meV [22] to the experimental data for FXA and FXB, respectively.

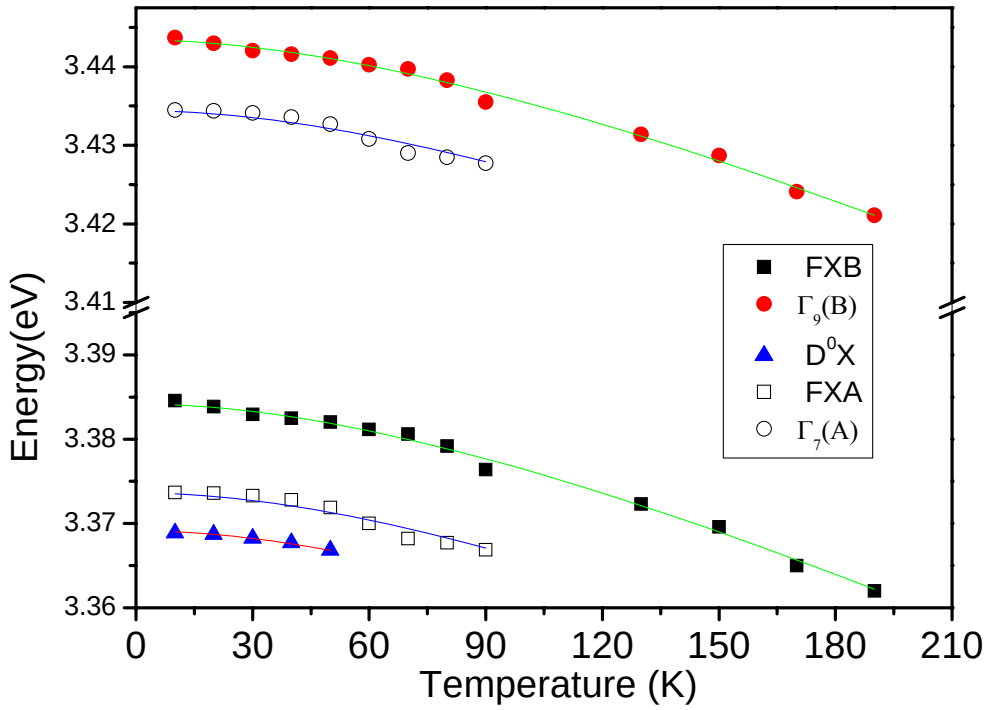

Figure 4.15-The energy bandgap and PL peak position as a function of temperature.

The solid lines in figure 4.15 represent the curve plotted by the varshni equation and fits well with obtained data. The best fit for the FX emission lines as well as the bandgap were obtained at $\alpha = 2.5\times10^{-4}\, eV/K$ and $\beta = 220\pm90\, K$ for the constants in equation 2.1. With these fit parameters, the values of $E(0)$ corresponding to D^0X, FXA and FXB are estimated as 3.369 eV, 3.375 eV and 3.384 eV, respectively. Moreover, the bandgap energy $E_g(0)$ with reference to valence band A and B were estimated as 3.434 eV and 3.443 eV, respectively. These values are in agreement with literature values reported for bulk ZnO as well as nanorods [10,22,49]. Moreover, the obtained values of the coefficients α and β in this work are in the range of previously reported literature values as shown in table 4.2.

Table 4.2-Coefficients for the temperature dependence of the exciton emissions and bandgap in various forms of ZnO (using Varshni equation).

Sources	α **(eV/K)**	β (K)
This work	2.5×10^{-4}	220 ± 90
Bulk ZnO [22]	5.7×10^{-4}	420
Single crystal ZnO[49]	1×10^{-3}	900
ZnO nanorods [10]	6×10^{-5}	240 ± 40

Despite the extensive studies of fundamental properties of luminescence in ZnO, the origin of the room temperature PL was among the challenging issues for several decades. Therefore, it is essential to present the room temperature PL of our nanowires as well. A typical room temperature micro-PL spectrum of the as-grown nanowires in the near band-edge region is shown in Figure 4.16.

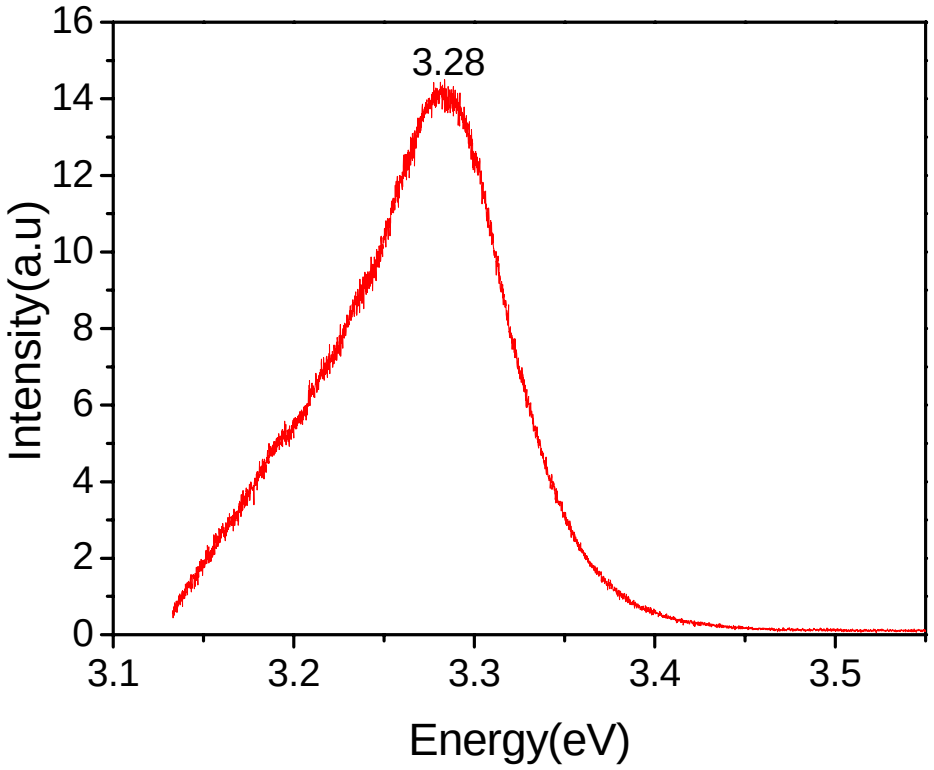

Figure 4.16-Typical room temperature micro-PL spectrum of as-grown ZnO nanowires measured using He-Cd (325 nm) laser excitation.

The spectrum exhibits a peak at 3.28 eV with line width of 49.4 meV. This peak is located at slightly higher energy than the previous reports for single crystalline ZnO nanorods [10]. Referring to the size distribution of the nanowires, the slight shift in energy could be due to little contribution from quantum confinement as presented for ZnO nanowires and nanorods in which the diameter exceeds 20 nm [44,48]. Nevertheless, the peak position at 3.28 eV is quite less than the expected value of free exciton transition energy 3.31 eV, if the widely accepted room temperature bandgap of 3.37 eV and binding energy of 60 meV for ZnO is used. These clearly indicate that the optical transition process responsible for the near band-edge PL of the nanowires at room temperature is not only from free excitonic emission, rather a superposition of multiple peaks from free exciton and their phonon replicas as well as residual bound exciton emission. It can be also evidentially supported by the temperature evolution of the various emission lines arising from the radiative decay of various excitons and their phonon replica with temperature as shown in figure 4.13.

CHAPTER 5: Conclusions and future outlook

5.1 Conclusions

Zinc oxide, with direct bandgap (3.37 eV) at RT, high free exciton binding energy (60 meV), and high thermal and mechanical stabilities has been recognized as a promising candidate for UV light emitters, transparent light power electronics, sensors, electro-mechanical coupled devices, and so on. In addition, one-dimensional nanostructures including nanowires are ideal candidates for understanding fundamental phenomena in low dimensional systems as well as for developing new generation nanodevices with high performance. A variety of techniques such as, MOCVD, CVD, MBE, porous template method, Laser ablation, and thermal evaporation and condensation have been used to synthesise one dimensional nanostructures of ZnO.

In this thesis, ZnO nanowires were synthesized on alumina substrate using a simple thermal evaporation method at ambient pressure without use metal catalysts. This technique has the advantage of simplicity, low cost, and less number of necessary apparatus than other techniques so far used for the synthesis of one-dimensional nanostructures. The as-synthesized nanowires were characterized structurally and optically using scanning electron microscopy, X-ray diffraction, Raman spectroscopy in resonant and nonresonant mode and photoluminescence.

Based on the observed morphology of the as-grown sample, we suggested that the growth process is occurring in two steps. When the furnace is heated to the growth temperature, the vapour from zinc powder (melting point = 419.6ºC) in the boat is transferred to the substrate through the nitrogen carrier gas. Meanwhile, the vapour from sprinkled zinc powder on the substrate also increases. These results in high supersaturation which leads to the formation of the bulk ZnO observed at the base of nanowires. After bulk ZnO at the base is formed and the growth temperature is attained, zinc vapour comes only from the source in the boat at a constant rate and results in lower supersaturation. This decrease in supersaturation combined with the anisotropy in surface energy leads to growth of nanowires. The growth process in our synthesis setup (ambient pressure and catalyst-free)

was enhanced by creating sharp temperature gradient (over short distance) between the source material in the boat and the substrate. SEM observation of the as-grown nanowires reveals that no metal particles or other impurities were detected in the growth front of the nanowires. Therefore, we conclude that the growth of nanowires obtained in this synthesis is controlled by the vapor-solid (VS) method rather than the vapor-liquid-solid (VLS) mechanism, which is common in catalyst-assisted methods.

The obtained XRD pattern of the as-grown sample is typically similar to the peaks indexed for wurtzite hexagonal phase of bulk ZnO. Moreover, except the peaks from the substrate no diffraction peaks corresponding to other phases such as unreacted Zn or other impurities were observed in XRD pattern. The nonresonant Raman spectra of as-grown nanowires exhibited sharp and intensive peak at 436.8 cm^{-1} corresponding to the Raman active $E_2(high)$ phonon mode of ZnO. The typical UV resonant Raman spectra of the nanowires also showed peaks at 570 cm^{-1} and 1145 cm^{-1} corresponding to the 1LO and 2LO phonon modes in ZnO. These XRD and Raman scattering measurement results confirmed that the as-grown nanowires exhibit wurtzite hexagonal phase with good crystal quality.

PL spectra of the nanowires were investigated both at low temperature and room temperature with above bandgap excitation. The low temperature (10K) PL showed fine structures in the near band-edge region and relatively week green emission band centred at ~2.4 eV. The green band referred as deep-level emission has been associated with structural defects (dominant in bulk ZnO) and recombination at surface states (mainly in low-dimensional structures with increased surface to volume ratio). The observed weak deep-level emission band relative to the near band-edge emission is an indication of reduced deep defects in the nanowires.

The near band-edge low temperature PL spectrum of the nanowires excited at 325 nm is dominated by sharp donor bound exciton emission at 3.369 eV. The free exciton emission line at 3.374 eV is also observed at low temperature. Moreover, the free exciton phonon replicas and the TES of donor bound exciton are observed in the range of 3.336-3.304 eV. The DAP emission band is observed at 3.247 eV. The optical data, mainly the observation of free exciton peak at low temperature (10K), strongly suggests that the nanowires are of

high optical quality. It has been proposed that defect-induced PL peaks are more dominant for the nanowires with high aspect ratio than those of bulk materials. However, the result obtained for the nanowires demonstrated that low defect concentration is still achievable for nanoscale materials in spite of the unfavourable conditions. The high optical quality of the nanowires in this work apparently results from their catalyst-free growth which excludes possible incorporation of catalytic impurities. Moreover, the nanowires were grown at relatively low temperature ~618ºC. Therefore, considerable reduction of defect concentration might have ensured since defect concentration, in general decreases exponentially with decreasing growth temperature.

The temperature dependent PL analysis of the nanowires showed that the free excitonic emission lines shift to lower energy with increasing temperature, and room temperature micro-PL spectrum showed a peak at 3.28 eV. The peak is slightly shifted to lower energy than the expected value of 3.31eV if we consider the bandgap of 3.37 eV and free exciton binding energy of 60 meV. This leads to a conclusion that the room temperature UV emission of the nanowires involves a contribution from free exciton and their phonon replica as well as the residual emission from the bound exciton.

5.2 Future outlook

ZnO nanostructures have been demonstrated as promising candidates for applications in nanosized electronic, optical, sensor, and optoelectronic devices. Undoubtly, detailed understanding of the growth mechanism(s) of the nanostructures and controlling of the processing parameters is the key to the development of these nano-scale devices.

Our result suggests that good crystal and optical quality ZnO nanowires can be synthesized on alumina substrate using a simple and cost effective thermal evaporation technique under ambient pressure without use of metal catalyst. However, the growth process can be affected by several factors including carrier gas flow rate, oxygen availability, temperature, distance between source material and substrate, etc which needs to be optimized in order to synthesis the nanowires reproducibly in large scale. The growth process in this work was enhanced by creating sharp temperature gradient between the source material and substrate

(over short distance), which was assured by keeping the alumina tube on the substrate side open to air. However, it was challenging to persistently control the temperature gradient under this setup. This could be due to the variation in external atmosphere on the open side of alumina tube. For reproducible synthesis of the nanowires, improvements to the synthesis setup can be made by closing both side of the tube during the growth process and using cooling system on the substrate side which favour the sharp temperature gradient. On the other hand, this may require readjustment of the other parameters as well.

Low temperature PL of the as-synthesised nanowires reveal a fine structured near band-edge emission lines with a relatively weak and broad green emission band. So far, there is no clear cut conclusion on the chemical nature of the center responsible for the green emission line as some attribute to the native defects such as oxygen vacancy and zinc interstitials while others assign to the copper impurity. Therefore, it is worthy to use other characterization techniques in addition to PL to understand the chemical nature of the centres responsible for this emission line. With this understanding it will be possible to control the introduction of the centres to the nanowires either during processing or by post treatment.

ZnO is known to be host candidate for rare earth (RE) ions doping. The RE ions give fluorescence spectra with sharp lines in the visible or neighbouring spectral regions, which is an important property for optoelectronic applications. These ions can be introduced to ZnO nanowires using simultaneous evaporation of ZnO powder and RE metal (oxide) under our experimental procedure. Furthermore, ZnO is found to be promising host material for ferromagnetic doping. Therefore, one can also incorporate magnetic ions such as Mn, Co, Fe into ZnO nanowires by using the simple thermal evaporation technique. This will facilitate the use of magnetic ZnO nanowires for developing of spin based nanodevices.

Appendix 1- Structural and Optical properties of the alumina substrate

Aluminium oxide has several different phases. The most stable one is $\alpha - Al_2O_3$ (sapphire). The Bravais lattice of sapphire is hexagonal close-packed (hcp) with lattice constants of $a = 0.475\ nm$ and $c = 1.3\ nm$ [2]. Sapphire has a wide bandgap of 9.1eV at room temperature which enables the material to transmit light over wavelength range from 150 nm to 5000 nm [50]. The melting point of sapphire is 2040ºC, and it has extremely high chemical stability even at higher temperature.

The hexagonal structure of sapphire combined with its chemical stability makes the material to be the top choice of substrates for growth of other hexagonal materials such as GaN, ZnO, AlN, and so on. The technological development of sapphire and its availability with relatively low cost is also one of the reasons for its wide use as substrates in spite of lattice mis-match. The high chemical stability can effectively reduce interface reaction between the sample and sapphire substrate so that the sample can be grown with high crystalline quality. Moreover, the large bandgap of sapphire makes optical characterization of samples grown on it to be carried out with insignificant disturbances.

The phase of alumina substrate, which was used to grow ZnO nanowires in this thesis work, was identified using XRD measurement as $\alpha - Al_2O_3$. The XRD pattern taken from the back surface of the substrate is shown in figure A.1 (a). Vibrational modes of the substrate were also investigated using UV Raman scattering. Figure A.1 (b) shows the Raman spectra obtained using He-Cd (325 nm) laser excitation. The observed peaks are coincident with the expected modes for $\alpha - Al_2O_3$ crystalline phase [51].

With 325nm laser excitation the spectrum of the studied samples also evidenced the presence of optical active centres in the near infrared spectral region (1.6-1.9 eV) as shown in figure A.2. Chromium, titanium and iron are common impurities in $\alpha - Al_2O_3$.These transition metal ions were known to give rise for luminescence band in the aforementioned spectral range [52-54]. A comparison of the measured PL with literature reports suggest that the ~1.83 eV and ~1.79 eV lines could be addressed to Fe^{3+} and Cr^{3+} in an alumina substrate, respectively [53,55].

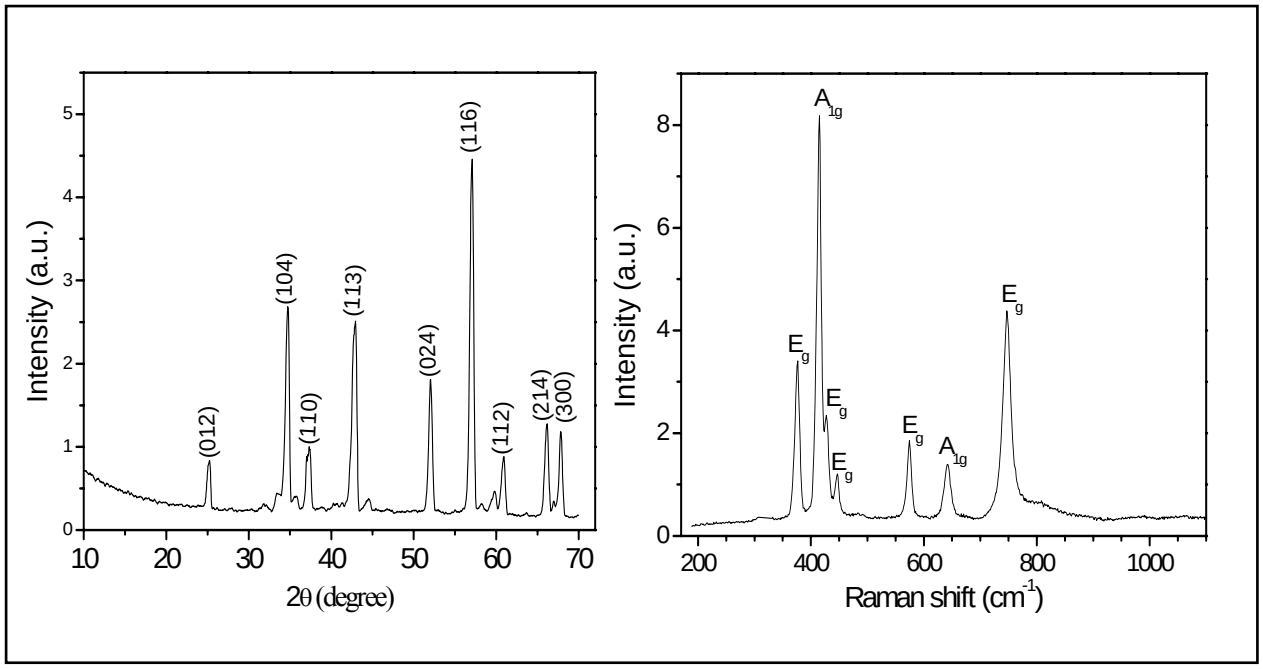

Figure A.1- (a) XRD pattern of alumina substrate (indexed in accordance with JCPDS, file 10-0173 (1996)), (b) Raman modes of alumina substrate with 325 nm laser excitation.

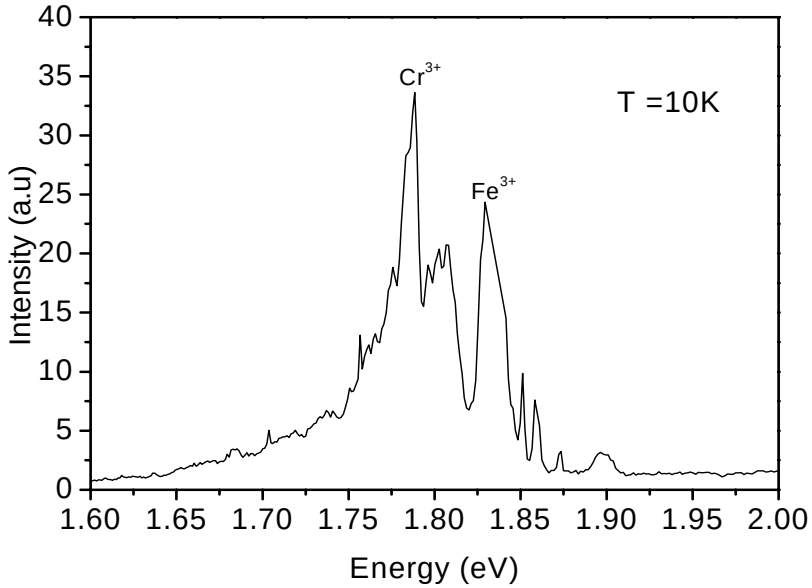

Figure A.2- Low temperature (10K) PL spectrum (in the near infrared region) of as-grown sample on alumina substrate obtained with 325nm laser excitation.

References

[1] Z. L. Wang, "Zinc oxide nanostructures: growth, properties, and applications", *Journal of Physics: Condensed matter*, 16, R829-R858 (2004).

[2] Z. Fan and J. G. Lu, "Zinc Oxide Nanostructures: Synthesis and Properties", *Journal of Nanoscience and Nanotechnology*, 5, 1561-1573 (2005).

[3] P. Yang, H. Yan, S. Mao, R. Russo, J. Johnson, R. Saykally, N. Morris, J. Pham, R. He, and H.-J. Choi, "Controlled Growth of ZnO Nanowires and Their Optical Properties", *Advanced Functional Materials*, 12 (5), 323-330 (2002).

[4] Z. L. Wang, "The new field of piezotronics", *Materialstoday*, 10(5), 20-28 (May 2007).

[5] A. B. Djuris˘ic and Y. H. Leung, "Optical Properties of ZnO Nanostructures", *Small* 2006, 2 (8-9), 944- 961 (2006).

[6] D. Banerjee, J. Y. Lao, D. Z. Wang, J. Y. Huang, Z. F. Ren, D. Steeves, B. Kimball, and M. Sennett, "Large-quantity free-standing ZnO nanowires", *Applied Physics Letters*, 83(10), 2061-2063 (2003).

[7] Y. Zhang, N. Wang, S. Gao, R. He, S. Miao, J. Liu, J. Zhu, and X. Zhang, "A simple method to synthesise nanowires", *Chemistry of Materials*, 14, 3564-3568 (2002).

[8] H. Fu, H. Li, W. Jie, and C. Zhang, "The O_2-dependent growth of ZnO nanowires and their photoluminescence properties", *Ceramics International*, 33, 1119-1123 (2007).

[9] A. Umar, Y. H. Im, and Y. B. Hahan, "Evolution of ZnO Nanostructures on Silicon Substrate by Vapor-Solid Mechanism: Structural and Optical Properties", *Journal of Electronic Materials*, 35(4), 758-765 (2006).

[10] A. Umar, B. Karunagaran, E-K. Suh, and Y. B. Hahn, "Structural and optical properties of single-crystalline ZnO nanorods grown on silicon by thermal evaporation", *Nanotechnology*, 17, 4072–4077 (2006).

[11] A. Khan, W. M. Jadwisienczak, H. J. Lozykowski, and M. E. Kordesch, "Catalyst-free synthesis and luminescence of aligned ZnO nanorods", *Physica E* 39, 258-261 (2007).

[12] A. Umar, S.H. Kim, J.H. Kim, and Y.B. Hahn, "Structural and optical properties of ZnO nanostructures grown on silicon substrate by thermal evaporation process", *Materials Letters*, 62, 167-171 (2008).

[13] Ü. Özgür, Y. I. Alivov, C. Liu, A. Teke, M. A. Reshchikov, S. Doğan, V. Avrutin, S.-J. Cho, and H. Morkoç, "A comprehensive review of ZnO materials and devices", *Journal of Applied Physics*, 98, 041301-1- 041301-103, (2005).

[14] Z. L. Wang, "Nanostructures of Zinc Oxide", *Materialstoday,* 26-33 (June, 2004).

[15] C. Jin, "*Growth and Characterization of ZnO and ZnO-Based Alloys_ $Mg_xZn_{1-x}O$ and $Mn_xZn_{1-x}O$", Ph.D. Dissertation*, North Carolina State University, 2003.

[16] C. Klingshirn, "ZnO: From basics towards applications", *physica status solidi (b)-basic research*, 244(9), 3027– 3073 (2007).

[17] K. A. Alim, V. A. Fonoberov, M. Shamsa, and A. A. Balandin, "Micro-Raman investigation of optical phonons in ZnO nanocrystals", *Journal of Applied Physics*, 97, 124313 (2005).

[18] S. Shionoya and W.M. Yen (Eds.), *Phosphor Handbook*, Phosphor Research Society, CRC Press, 1998.

[19] C.F. Klinghirn, *Semiconductor Optics*, Springer. Germany 1995.

[20] B. K. Meyer, H. Alves, D. M. Hofmann, W. Kriegseis, D. Forster, F. Bertram, J. Christen, A. Hoffmann, M. Straßburg, M. Dworzak, U. Haboeck, and A. V. Rodina, "Bound exciton and donor–acceptor pair recombinations in ZnO", *physica status solidi (b)-basic research,* 241(2), 231– 260 (2004).

[21] H. Y. Fan, "Temperature Dependence of the Energy Gap in Semiconductors" *Physical Review*, 82(6), 900-905 (1951).

[22] C.J. Youn, T.S. Jeong, M.S. Han, and J.H. Kim, "Optical Properties of Zn-terminated ZnO bulk", *Journal of Crystal Growth*, 261, 526-532 (2004).

[23] R. R. L. Seitz, "*Optical characterization of Cubic and Hexagonal GaN" Ph.D. Dissertation*, Universidade de Aveiro, 2000.

[24] H. H. Choi, "*Synthesis and characterization of Tailored Zinc Oxide Nanostructures and Their Engineered Nanocomposites*" Ph. D. Dissertation, University of Florida, 2004.

[25] P. X. Gao and Z. L. Wang., "Nanoarchitectures of semiconducting and piezoelectric zinc oxide", *Journal of Applied Physics*, 97, 044304 (2005).

[26] X.Y. Kong and Z. L. Wang, "Spontaneous Polarization-Induced Nanohelixes, Nanosprings, and Nanorings of Piezoelectric Nanobelts", *Nano Letters*, 21(3), 1625-1631 (2003).

[27] G. Cao. *Nanostructures & nanomaterials; Sysnthesis, Properties & Application.* Washington, Imperial Collage Press, 2004.

[28] W. L. Hughes, "*Synthesis and Characterization of zinc oxide nanostructures for Piezoelectric Applications*", Ph.D. Dissertation, Georgia Institute of Technology, December 2006.

[29] X. Zhang, L. Wang, and G. Zhou, "Synthesis of well-aligned ZnO nanowires without catalyst", *ReviewAdvanced Materials Science*, 10, 69-72 (2005).

[30] X.Q. Meng, D.Z. Shen, J.Y. Zhang, D.X. Zhao, Y.M. Lu, L. Dong, Z.Z. Zhang, Y.C. Liu, X.W. Fan, "The structural and optical properties of ZnO nanorod arrays", *Solid State Communications*, 135, 179–182 (2005).

[31] H.Y. Wei, G.W. Cong, P.F. Zhang, W.G. Hu, J.J. Wu, C.M. Jiao, X.L. Liu, Q.S. Zhu, and Z.G. Wang, "Combined structure of ZnO vertical well-aligned nanorods and net-like structures on AIN/sapphire", *Journal of Crystal Growth*, 306, 12–15 (2007).

[32] I. R. Lewis and H. G. M. Edwards, (Eds.), *Handbook of Raman spectroscopy: from the research laboratory to the process line*, practical spectroscopy series 28, New York, Marcel Dekker, Inc, 2001.

[33] J. Jie, G. Wang, Y. Chen, X. Han, Q. Wang, B. Xu, and J. G. Hou, "Synthesis and optical properties of well-aligned ZnO nanorod array on an undoped ZnO film", *Applied Physics Letters*, 86, 031909 (2005).

[34] L. Bergman, X.-B. Chen, J. Huso, J. L. Morrison, and H. Hoeck, "Raman scattering of polar modes of ZnO crystallites", *Journal of Applied Physics*, 98, 093507 (2005).

[35] J. F. Scott, "UV Resonant Raman Scattering in ZnO", *Physical Review B*, 2(4), - (1970).

[36] H. T. Ng, B. Chen, J. Li, J. Han, M. Meyyappan, J. Wu, S. X. Li, and E. E. Haller, "Optical properties of single-crystalline ZnO nanowires on m-sapphire", *Applied Physics Letters*, 82(13), - (2003).

[37] H. -M. Cheng, H. -C. Hsu, Y. -K. Tseng, L.-J. Lin, and W.-F. Hsieh, "Raman Scattering and Efficient UV Photoluminescence from Well-Aligned ZnO Nanowires Epitaxially Grown on GaN Buffer Layer", *Nanotechnology*, **17,** 4072-4077 (2006).

[38] M. Fox, *Optical Properties of Solids*, Oxford University press, 2001.

[39] B. Henderson and G. F. Imbusch, *Optical Spectroscopy of Inorganic Solids*, Oxford, Clarendon press, 1989.

[40] S.A. Studenikin, M. Cocivera, W. Kellner, and H. Pascher, "Band-edge photoluminescence in polycrystalline ZnO films at 1.7K", *Journal of Luminescence*, 91, 223-232 (2000).

[41] T. Monteiro, A. J. Neves, M. C. Carmo, M. J. Soares, M. Peres, J. Wang, E. Alves, E. Rita, and U. Wahl, "Near-band-edge slow luminescence in nominally undoped bulk ZnO", *Journal of Applied Physics*, 98, 013502 (2005).

[42] B. K. Meyer, J. Sann, D. M. Hofmann, C. Neumann and A. Zeuner, "Shallow donors and acceptors in ZnO", *Semiconductor Science and Technology*, 20, S62–S66 (2005).

[43] B. K. Meyer, J. Sann, S. Lautenschläger, M. R. Wagner, and A. Hoffmann, "Ionized and neutral donor-bound excitons in ZnO", *Physical Review B*, 76, 184120 (2007).

[44] H. C. Hsu and W.F. Hsieh, "Excitonic polaron and phonon assisted photoluminescence of ZnO nanowires", Solid State Communications, 131, 371-375 (2004).

[45] X. Meng, D. Zhao, D. Shen, J. Zhang, B. Li, X. Wang, X. Fan, "ZnO nanorod arrays grown under different pressures and their photoluminescence properties", *Journal of Luminescence*, 122-123, 766-769, (2007).

[46] T. Monteiro, C. Boemare, and M. J. Soares, "Photoluminescence and damage recovery studies in Fe-implanted ZnO single crystals", *Journal of Applied Physics*, 93(11), 8995-9000 (2003).

[47] T. Monteiro, A. J. Neves, M. C. Carmo, M. J. Soares, M. Peres, E. Alves, E. Rita, and U. Wahl, "Optical and structural analysis of bulk ZnO samples undoped and rare earth doped by ion implantation", *Superlattices and microstructures*, 39, 202-210 (2006

[48] W. I. Park, Y. H. Jun, S. W. Jung, and G.-C. Yi, "Excitonic emissions observed in ZnO single crystal nanorods", *Applied Physics Letters*, 82 (6), 964-966 (2003).

[49] V. V. Ursaki, I. M. Tiginyanu, V. V. Zalamai, and E. V. Rusu, "Multiphonon resonant Raman scattering in ZnO crystals and nanostructured layers", *Physical Review B*, 70, 155204 (2004).

[50] http://www.crystalsystems.com/sapphys.html

[51] S. S. S. Porto and R. S. Krishnan, "Raman Effect of Corundum", *Journal of Chemical Physics*, 47, 1009-1012 (1967).

[52] S.V Bulyarskii, A.E. Kozhevin, S.N. Mikov, and V.V.Prikhodko, "Anomalous R-line behaviour in nanocrystalline Al_2O_3: Cr^{3+} ", *Physica status solidi (a)*, 180, 555 (2000).

[53] T. Monteiro, C. Boemare, M. J. Soares, E. Alves, C. Marques, C. McHargue, L. C. Ononye, and L. F. Allard "Luminescence and structural studies of iron implanted $\alpha - Al_2O_3$", *Nuclear Instruments and Methods in Physics Research B*, 191, 638-643 (2002).

[54] B. F. Gachter and J. A. Koningstein, "Zero phonon transition and Jahn-Teller phonon energies from the fluorescence spectrum of $\alpha - Al_2O_3$: Ti^{3+} ", *Journal of chemical,* 60(5), 2003 (1974).

[55] T. Li, S. Yang, L. Huang, J. Zhang, B. Gu, and Y. Du, "Strong photoluminescence from Cr^{3+} doped porous anodic alumina", *Journal of Physics: Condensed Matter*, 16, 2463-2469, (2004).